USING A BIMODAL SIZE DISTRIBUTION TO RETRIEVE MARINE LOW CLOUD PROPERTIES USING A-TRAIN SATELLITE AND GROUND DATA

by

Tyler K. West

A thesis submitted to the faculty of
The University of Utah
in partial fulfillment of the requirements for the degree of

Master of Science

Department of Atmospheric Sciences

The University of Utah

August 2014

The University of Utah Graduate School

STATEMENT OF THESIS APPROVAL

The following faculty members served as the supervisory committee chair and members for the thesis of **Tyler K. West**

Dates at right indicate the members' approval of the thesis.

Gerald G. Mace, Chair	4/17/14 Date Approved
Edward J. Zipser, Member	4/17/14 Date Approved
Steven K. Krueger, Member	4/17/14 Date Approved

The thesis has also been approved by **Kevin D. Perry**

Chair of the Department of **Atmospheric Sciences**

and by David B. Kieda, Dean of The Graduate School.

ABSTRACT

Understanding the connection between large-scale meteorology, cloud macrophysical variables, and cloud microphysical variables is needed in order to improve the parameterization of marine boundary layer (MBL) clouds in weather and climate models. For this study, multiple aspects of MBL clouds over the Atmospheric Radiation Measurement Program (ARM) mobile site at Graciosa Island, Azores are examined. Hourly averaged raw variables of cloud fraction, column summed dBZ, liquid water path, first cloud base height, boundary layer static stability, and midtropospheric static stability are clustered together using a K-means clustering algorithm. The cluster output infers seven characteristic cloud regimes that describe the spectrum of warm boundary layer clouds that occurred over Graciosa Island during the deployment. These cloud regimes range from precipitating stratocumulus to nonprecipitating fair weather cumulus to deep clouds associated with broad synoptic scale frontal systems. Using the cluster results and NCEP/NCAR reanalysis, the typical macrophysical and meteorological environments for the MBL cloud regimes are summarized along with their average radar profiles. MBL cloud microphysical properties are then derived using a new retrieval algorithm that assumes the presence of both cloud and precipitation particle modes within a radar resolution volume. Compared to a traditional single mode particle size distribution (PSD), a bimodal PSD is closer to in-situ observations and is expected to provide improved statistics and understanding of the cloud microphysical parameters

such as number concentration, precipitation rate, and effective droplet sizes. The bimodal retrieval algorithm can use either ARM ground-based or A-Train satellite-based data as an input. This study finds that ARM and A-Train versions of the bimodal algorithm retrieve plausible microphysics and the reasons for their differences are explored. Case studies are completed using the bimodal retrieval for three shallow cloud regimes with varying precipitation, macrophysical, and synoptic environments. Results show that microphysical quantities do change as the cloud regime varies and validate the connection between the large and small-scale environment of MBL clouds. The specifics of the unique regime-based microphysics are also useful in order to better parameterize these clouds in models.

TABLE OF CONTENTS

ACKNOWLEDGEMENTS

I thank my graduate advisor and committee chair, Dr. Jay Mace, for his guidance and knowledge along with the output of his retrieval algorithm. I also thank my committee members, Dr. Ed Zipser and Dr. Steve Krueger, for their availability and feedback. Comments from Janna West, Leah Campbell, and Betsy Berry improved the manuscript. Troubleshooting and advice from Stephanie Avey, Sally Benson, Betsy Berry, and members of the Mace Group were essential to the completion of this thesis. Support and encouragement from fellow graduate students is also very appreciated. Data and computational time were made available by the Department of Energy's ARM program, NASA's A-Train program, NCEP/NCAR, and the University of Utah Center for High Performance Computing. This work is funded by the United States Air Force and the views expressed in this thesis are those of the author and do not reflect the official policy or position of the United States Air Force, Department of Defense, or the U.S. Government.

CHAPTER 1

INTRODUCTION

Warm marine clouds that form within the boundary layer play a critical and dominant role in the earth's climate system as they impact both energy and water budgets as well as the general circulation. These clouds are often referred to as Marine Boundary Layer (MBL) clouds and examples include shallow cumulus (Cu), stratocumulus (Sc) and stratus (St). MBL clouds occur frequently over the global oceans, as observed by A-Train satellites in Figure 1. In addition, Hahn and Warren (2007) calculate that marine low clouds have a global ocean annual average cloud amount of 55%, comprising the largest amount of cloud cover by level. The large coverage and impact on the energy budget of MBL clouds mean that even small changes in their coverage and properties result in a radiative effect similar in magnitude to that associated with greenhouse gas increases (Randall et al. 1984; Slingo 1990). Sadly, global climate models (GCM) vary widely in their representation of the coverage and properties of MBL clouds [Intergovernmental Panel on Climate Change (IPCC) 2013)].

MBL clouds are key to the earth's radiation budget because they act as regulators for the amount of solar energy that reaches the surface (Hartmann et al. 1992; Chen et al. 2000). This occurs as changes in cloud microphysical quantities such as liquid water content (LWC), droplet size (r_e), and number concentration (N_d) are connected to changes in cloud macrophysical properties such as albedo, optical depth (τ), lifetime, and

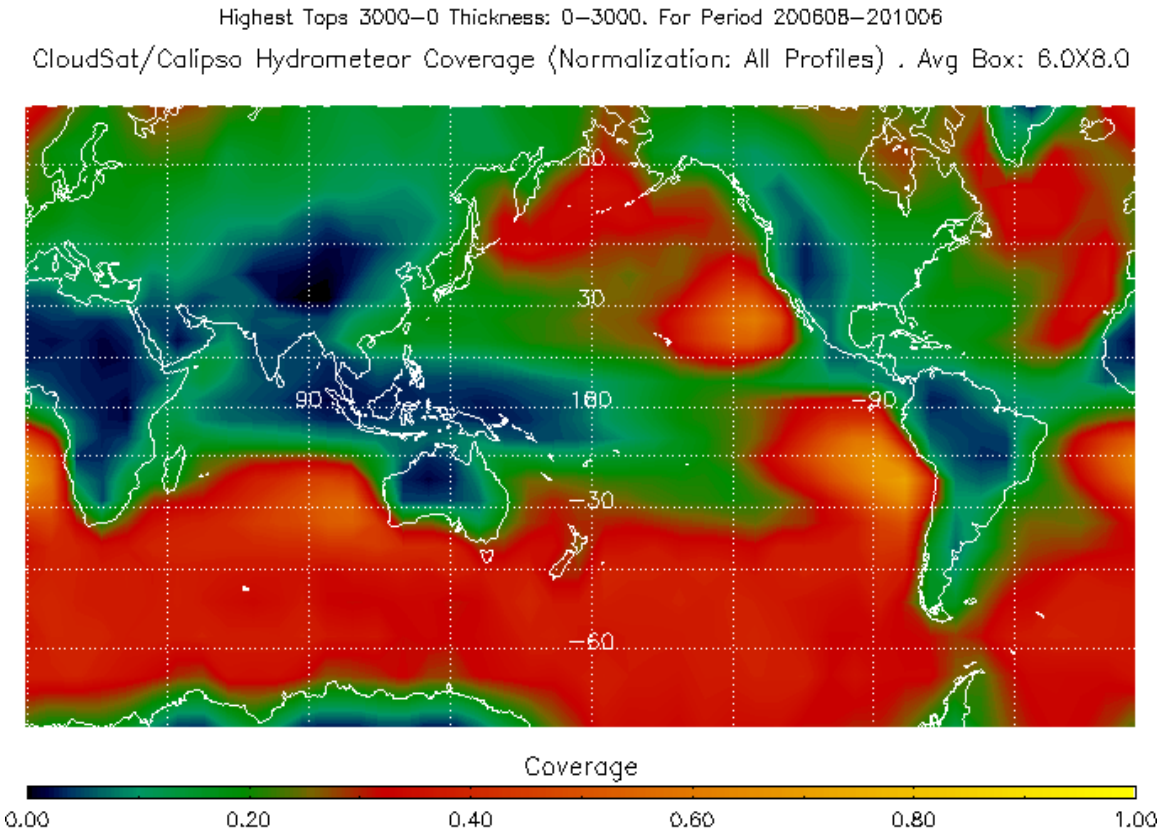

Figure 1. Global low-topped (tops < 3 km) cloud coverage fraction derived from A-Train member satellites using RL-GeoProf dataset. Period of observations: Aug 2006 to Jun 2010. Image courtesy of G.G. Mace.

coverage, which in turn impact absorbed radiation (Hartmann 1994; Iacobellis and Somerville 2000; Mace 2010). Cloud properties also vary by cloud type, resulting in different amounts of absorbed solar radiation at cloud top and at the surface when the three main types of low clouds are present (Wood and Hartmann 2006). Aerosols also regulate absorbed surface solar radiation as they act to alter MBL cloud properties such as albedo, precipitation, and lifetime (Sorooshian et al. 2009; Lee et al. 2012).

Another key aspect of MBL clouds is their impact on the water cycle (Snodgrass et al. 2009). Precipitation that falls from MBL clouds over the tropics and subtropics is often referred to as "warm rain" as all processes occur at temperatures warmer than 0° C. Studies have shown that some amount of warm rain is nearly always present in MBL clouds and that the warm rain that is able to reach the surface leads to a notable amount of global rainfall (Haynes and Stephens 2007; Lebsock et al. 2011). Liu and Zipser (2009) used TRMM data to find that warm rain is responsible for 20% of total rainfall throughout tropical oceans. A-Train satellite data showed that in 2010, warm rain was responsible for 31% (Jan) and 35% (Jul) of global rain occurrence (Chen et al. 2011). TRMM warm rain estimates are lower than those of the A-Train due to the TRMM radar's relatively high minimum detectable signal of roughly 17 dBZ, causing TRMM to not detect much of the Earth's warm rain occurrence. In addition to the direct impact on the water cycle, the mere formation of warm rain in MBL clouds has also been shown to alter low cloud organization by decreasing coverage and lifetime, which in turn impacts cloud albedo and absorbed solar radiation (Sharon et al. 2006; Wood et al. 2009).

MBL clouds also play a key role in the general circulation of the atmosphere (Stevens 2005). As initially explained by Riehl et al. (1951), MBL clouds play the

primary role in moistening and expanding the depth of the trade wind layer from east to west, promoting deeper convection. In addition, marine low clouds can impact the strength of trade winds and help control sea surface temperatures (http://www.arm.gov/sites/amf/grw/). Atmospheric circulation is also enabled as MBL Cu clouds transport water vapor from the MBL into the free atmosphere (Ghate et al. 2011). Combined, these factors feed the hydrological cycle and drive the rate of surface evaporation in trade wind-affected areas (Rauber et al. 2007).

Although MBL clouds play a major and key role in the energy and water budgets of the atmosphere, low clouds are not entirely understood and their feedbacks are the largest source of uncertainty in Global Climate Model (GCM) predictions of climate change (Dufresne and Bony 2008; Clement et al. 2009; Lin et al. 2014). The primary source of this uncertainty comes from varying cloud coverage forecasts, as some GCMs increase MBL cloud coverage under warming while other models decrease coverage (Bony and Dufresne 2005). This leads to a factor-of-five disparity between different GCMs regarding their coverage of low clouds under increases in global temperatures (Soden and Held 2006). Of particular concern is the poor coverage of MBL clouds by models in the present climate, let alone in a changed climate (Williams and Tselioudis 2007; IPCC 2013). For this reason, a better understanding of cloud properties and their relation to the large-scale environment should help to improve low cloud representation in current and future forecasts.

Model discrepancies regarding the present and future of low clouds can arise due to the first and second aerosol indirect effects. In general, the interaction of aerosols with MBL clouds has been an area of much research and debate. The widely accepted first

indirect effect proposed by Twomey (1977) is that higher aerosol concentrations create more droplets per unit volume and lead to brighter clouds that reflect more incoming radiation (for a fixed LWP). The second indirect effect, put forth by Albrecht (1989), is that higher droplet concentrations cause smaller droplets that suppress the formation of rainfall. This in turn increases cloud lifetime, which also acts as a negative radiation feedback. By extension, nonprecipitating clouds with higher droplet concentrations will also be more reflective than precipitating clouds (Savic-Jovcic and Stevens 2008). In general, models tend to produce results consistent with these theories (e.g., Jiang et al. 2010). However, observational evidence does not always confirm the veracity of these model forecasts (Lee et al. 2012). One reason observations do not agree with model output might be the large number of internal feedbacks among both the microphysics and dynamics of these clouds, which could lead to a reduction in the ability of the aerosols to impact convective low clouds and therefore effectively neutralize the effect of aerosol fluctuations (Stevens and Feingold 2009). Due to this discrepancy, further research is needed to understand the interaction of both cloud microphysics and macrophysics with aerosols.

Another reason for discrepancies among models and between models and observations is that GCM parameterizations for both the processes and time scales of warm rain and droplet growth are inadequate, which stems in part from an incomplete understanding of warm rain (Stephens et al. 2010). By definition, warm rain occurs when cloud droplets formed due to condensation grow to become raindrops through the collision-coalescence process (Liu and Zipser 2009). These processes are represented in most models by autoconversion and accretion. Autoconversion occurs when small cloud

drops self-collect and grow while accretion occurs when raindrops collect smaller cloud drops (Feingold et al. 2013). Of these two processes, accretion leads to the more rapid growth. However, there is some uncertainty regarding the processes used for cloud droplets to grow to a size where the collision-coalescence/accretion process can be initiated. Drops of this size are referred to as "collision-coalescence initiators" (CCIs) (Johnson 1993). Processes believed to create these CCIs include the presence of giant aerosols that lead to giant cloud condensation nuclei (CCN), the effects of turbulence and entrainment, and radiative broadening (Wallace and Hobbs 2006). During the RICO experiment, Small and Chung (2008) found evidence that entrainment near cloud top may create turbulence that will increase the local rate of collision-coalescence, leading to the formation of CCIs and rain. In addition, models often do not accurately predict the time scale of precipitation formation and frequently initiate precipitation much faster than observed (Suzuki et al 2011). This process has been observed to occur in as little as 10 minutes and usually averages 10-30 minutes (Small and Chuang 2008). Fluctuations to the timing of precipitation can cause changes to cloud lifetime and coverage as dictated by the second aerosol indirect effect.

Much work has been devoted to studying MBL clouds in order to improve their representation in GCM models. Field experiments such as the Clouds, Aerosol and Precipitation in the Marine Boundary Layer (CAP-MBL) and Variability of American Monsoon Systems (VAMOS) Ocean–Cloud–Atmosphere–Land Study Regional Experiment (VOCALS-Rex) have focused on low clouds over the northeastern Atlantic and southeastern Pacific (Rémillard et al. 2012; Mechoso et al. 2012). Campaigns such as the Rain in Cumulus over the Ocean (RICO) focused primarily on Cu clouds while the

Marine Stratus/Stratocumulus Experiment (MASE) focused on St and Sc (Rauber et al. 2007; Lu et al. 2009). Studies using satellite data to observe low cloud properties are numerous and include those by Liu and Zipser (2009), Kubar et al. (2009), Mace (2010), and Lebsock and L'Ecuyer (2011). Modeling studies such as those done by Wood et al. (2009), along with Bogenschutz and Krueger (2013), are aimed at improving model boundary layer cloud representations. Finally, cloud aerosol interactions have been a specific area of focus using both observations and model output (Sorooshian et al. 2009; Stevens and Feingold 2009).

Results from MBL cloud work indicate that at the heart of the factors that lead to GCM discrepancies is the incomplete understanding of MBL cloud microphysical and macrophysical properties (Dong and Mace 2003). Cloud microphysical properties also help determine the propensity of MBL clouds to form precipitation and help regulate cloud albedo (Wood 2005). For these reasons, the end goal of this study is to improve the understanding of MBL cloud properties for application into MBL cloud parameterizations in GCMs. This is done by first categorizing the cloud regime based on a combination of meteorological and cloud macrophysical parameters and second by utilizing a new and improved microphysical retrieval algorithm to study cloud microphysics of the regimes. This work is the first to utilize the new retrieval algorithm in order to compare the microphysical quantities of different cloud regimes.

Categorizing the cloud regime is a necessary first step because cloud macrophysical properties and microphysical quantities have been shown to depend on the cloud regime's cloud type and local meteorology (Wood and Hartmann 2006; Lacagnina and Selten 2013). Examples of this dependence include cloud coverage as shown by

Clement et al. (2009), cloud type as shown by Kiehl et al. (1994), and the long-standing relationship between cloud cover and lower tropospheric stability (LTS) (Klein and Hartmann 1993). In order to objectively categorize the hourly MBL cloud regime, a K-means cluster analysis methodology is adopted in this study with inputs from observed meteorological and cloud macrophysical variables. From the cluster analysis, multiple cloud regimes are inferred that describe the spectrum of MBL clouds over the Northern Atlantic. Additional understanding about the frequency, cloud height, and precipitation properties of these regimes and their respective cloud types is also gleaned from the cluster analysis. Using reanalysis data, the typical meteorological environments for these MBL cloud regimes are explored and compared across cloud regimes. Once it is known exactly when different cloud regimes occurred, MBL cloud microphysical properties can be derived based on cloud regime. This derivation utilizes a new retrieval algorithm developed by Dr. Jay Mace and assumes the presence of both cloud and precipitation particle size modes within the cloud. Compared to a traditional single mode particle size distribution (PSD), a bimodal PSD approach agrees more with observations and will allow for a more realistic retrieval of the average microphysical parameters and enable a microphysical comparison based on cloud regime (Fox and Illingworth 1997; Snodgrass et al. 2009). The algorithm can utilize observations from either ground-based or satellite-based remote sensors and microphysical output from these two categories of sensors is compared in this work. The end result of the new algorithm should improve statistics and understanding of the cloud microphysical parameters that are critical to the Earth's energy budget, water budget, and circulation. These statistics can help fulfill the overall goal of this work, which is to improve model forecasts of MBL clouds and precipitation.

CHAPTER 2

DATA

ARM CAP-MBL

Much of the data used for this study comes from the Atmospheric Radiation Measurement (ARM) CAP-MBL field campaign. Refer to Mather and Voyles (2013) for more information on the ARM program. The CAP-MBL campaign was based at the Graciosa Airport, Graciosa Island, Azores (39° 5' 28" N, 28° 1' 45" W), at an elevation of 15 m, and utilized ARM Mobile Facility (AMF) equipment to study cloud and precipitation properties of MBL clouds. This site will hereafter be referred to as GRW, which is the Graciosa Airport three letter identifier. Local standard time for the Azores is -1 UTC. The entire campaign lasted roughly May 2009 to Dec 2010 with cloud analysis sensors operating for approximately 19 months from Jun 2009 to Dec 2010. This relatively large time frame has created one of the most comprehensive MBL cloud datasets currently available.

Located in a remote location of the northeast Atlantic Ocean approximately 1600 km west of Portugal, Graciosa Island is ideal for sampling a wide variety of MBL clouds as it lies in the transition zone between extra and subtropical regimes. In fact, Dr. George Tselioudis recently found that the distribution of ISCCP Weather States over GRW is very similar to that of the global distribution of Weather States (Tselioudis 2014;

Wood et al. 2014). This makes the marine clouds over GRW a particularly good proxy for global marine cloud occurrence and also for cloud transitions between midlatitude and subtropical regimes. Climatologically, GRW low clouds are comprised mainly of clouds associated with frontal systems in the late fall, winter, and early spring. Clouds then transition to mostly stratocumulus in spring to early summer and finally to a broken trade cumulus regime in midsummer to early fall. MBL clouds occur frequently and are observed roughly 40% of the time during the winter and up to 60% in the summer and early fall (Rémillard et al. 2012, hereafter REM12). MBL clouds with tops below 3 km are responsible for 20% of the GRW annual surface precipitation. From Jun to Aug, clouds with tops below 4 km provide 50% of surface precipitation (Wood et al. 2014).

The Northeast Atlantic has previously been used to study the boundary layer and associated clouds beginning with the Atlantic Tradewind Experiment (ATEX) in 1969 (Augstein et al. 1973). The Atlantic Stratocumulus Transition Experiment (ASTEX) campaign focused on the transition from Sc to Cu and was based in the Azores in 1992 Albrecht et al. 1995). Important findings were made during the ASTEX campaign regarding the interaction of Sc and Cu over the marine environment (Miller and Albrecht 1995). Recent studies over the Azores which utilize the CAP-MBL data include a MBL cloud climatology in REM12, vertical motion characteristics of Cu by Ghate et al. (2011), and the use of CAP-MBL observations to improve low cloud representations in the ECMWF model (Ahlgrimm and Forbes 2013).

From among the suite of AMF sensors, the following were used for this study: W-Band ARM Cloud Radar (WACR), Vaisala Ceilometer, Microwave Radiometer (MWR), Sky Radiometers on Stand for Downwelling Radiation (SKYRAD), and radiosondes.

WACR

The WACR is a 95 GHz vertically pointing Doppler radar. Its relatively short wavelength enables sensitivity to cloud and precipitation drops down to -50 dBZ at 2 km and aids high spatial (43 m) and temporal (roughly 2 s) resolution. The WACR's temporal resolution is the shortest of all the instrumentation used in this test and was used as the baseline for the hourly temporal analysis. WACR Attenuation is minimal, but not negligible, for light to moderate precipitation. These factors combine to make the WACR very effective for observing the properties of MBL clouds (Mead and Widener 2005). These strengths also create limitations as very small cloud drops can be missed or heavy precipitation can attenuate the signal. One major WACR outage occurred for more than 22 days in Sep 2010. There were also six other outages that were much shorter and totaled less than 72 hours total time.

Vaisala Ceilometer

The CT25K ceilometer uses a 905 nm vertical laser pulse to measure the height of clouds above the surface (Nowak et al. 2008). REM12 point out that three layers can be detected but generally the first cloud base height (FCBH) is the most reliable due to attenuation of the laser. The ceilometer's temporal resolution is approximately 15 s and each measurement is assumed to be representative of the interim time. Range resolution for the ceilometer is 15 m. It was used during the entire CAP-MBL campaign with three outages lasting more than 24 hours and roughly 12 shorter outages.

MWR

The MWR passively measures emitted radiation from the atmosphere at 23.8 and 31.4 GHz in order to retrieve the amount of liquid water and water vapor in the column (Liljegren 2000; Westwater et al. 2003). Time resolution of the MWR is 30 s and each measurement represents the summation of emitted radiation during 20 s of that time. One limitation of the MWR is its lack of ability to accurately sense liquid water path (LWP) while the window of the instrument is wet. This occurs when precipitation reaches the ground and wets the radome protecting the instrument, resulting in anomalously high brightness temperatures. Data collected during these periods are flagged as "wet window" (http://www.arm.gov/publications/tech_reports/handbooks/mwr_handbook.pdf).

Overall, outages for the MWR were minimal throughout the campaign. However, there was a data processing problem that occurred from 11 July to 9 August 2010. Data collected during this time are available but it has been suggested by REM12 that they are unreliable. While some of the actual numerical values might be incorrect, what is important to this study is whether the value was comparatively low, midrange, or high. As there are no significant outliers from the normal mean during the data processing issue and values appear to be inline with other observations, the MWR observations for this time period are included in the cluster analysis portion of this study.

SKYRAD

The SKYRAD is a collection of radiometers used to measure downwelling shortwave and longwave radiative fluxes from clouds (Miller and Slingo 2007). Shortwave fluxes are generally transmitted while longwave infrared (IR) fluxes are emitted. Resolution on the SKYRAD is roughly 60 s as it collects data from the sensors.

In order to be used in this study, both the shortwave and longwave radiative fluxes must be available, meaning that only daytime data from the SKYRAD are used in this study. The SKYRAD operated throughout the campaign without any major outages.

Radiosondes

Radiosondes were launched every 6 hours daily beginning at approximately 0530 GMT. Standard thermodynamic and wind variables were measured at a vertical resolution of approximately 10 m. No radiosondes were launched during the period of 2 December 2009, 1200 UTC through 12 January 2010, 1200 UTC. Radiosonde data were not collected during two shorter periods of 21-22 June 2009 and 24-25 January 2010. On an additional 29 occasions, a balloon was either not launched or did not work. During these periods, data from the most representative radiosonde within 6 hours of the missing data were used with the assumption that the thermodynamic state of the atmosphere had not changed significantly. While during times of transition this assumption may not be accurate, the bulk nature and subsequent clustering of the data in this study significantly minimize the impact of this assumption.

A-Train

Data for this study also come from instruments onboard the polar orbiting A-Train member satellites (Stephens et al. 2002). The primary instrument used is the Cloud Profiling Radar (CPR) on *Cloudsat* (Im 2006; Mace et al. 2007). The CPR operates at 94 GHz with a footprint of roughly 1.5 km across-track and 1.7 km along-track. Vertical range bin resolution is 240 m and the minimum detectable signal is approximately -30 dBZ. Some optically thin Sc clouds might be missed due to the CPR minimum

detectable signal, but Fox and Illingworth (1997) suggest only 10-20% of these very thin Sc (LWP < 20 g m^{-2}) would be missed. Another limitation of the CPR is known as ground clutter, where the more reflective surface contaminates backscattered energy near the earth's surface. Due to this, CPR data below 500 m are not used and only precipitation-sized hydrometeors are detectable between roughly 500 m and 1000 m (Marchand et al. 2008). At 94 GHz, signal attenuation due to liquid water is present during periods of high liquid water path, which are normally associated with periods of moderate or greater liquid precipitation. Attenuation due to absorption at 94 GHz also means liquid water will emit a signal at this frequency. This signal is detectable within the CPR noise and will be discussed further in the methods section as it is used to determine the liquid water path within the CPR footprint.

The other instrument used from the A-Train is the Moderate Resolution Imaging Spectroradiometer (MODIS) onboard the *Aqua* satellite (Platnick et al. 2003). *Aqua* flies in formation just ahead of *Cloudsat*, allowing both sensors to observe nearly the same footprint. MODIS employs multiple bands in the visible and near IR, ranging from 0.46 to 3.75 micrometers, in order to observe cloud optical properties. MODIS is also used to gather information regarding aerosols, ocean color, and surface or vegetation properties. Because visible bands are used in this study to retrieve cloud properties, only daytime overpasses of *Aqua* and *Cloudsat* (crossing the equator at approximately 13:30 p.m. local time) are used. The longer MODIS wavelengths are better suited for deriving cloud properties near the top of the cloud while shorter wavelengths provide information from deeper within the cloud (Nakajima and Nakajima 1995).

ARM and A-Train Differences

While the A-Train has similar instruments as the WACR, MWR, and SKYRAD, there are inherent differences that result in strengths and weakenesses for the ground-based and satellite-based observing systems. First, the A-train looks down on the clouds while ARM looks up. Inherent to this difference is also the fact that the ARM sensors are much closer to the clouds compared to the A-train sensors. Looking down and being further away result in a major limitation of the A-Train not being able to detect cloud base as the lidar on board *CALIPSO* attenuates in optically thick clouds. Another result of the A-train looking down is the previously mentioned ground clutter, causing the CPR to not observe clouds below roughly 500 m and have limited utility between 500 m and 1000 m. While this does limit the ability of the A-train to observe low MBL clouds, looking down also provides a great benefit in that A-train continuously orbits the earth and covers a huge area compared to the fixed ARM sensors. The downside to quickly orbiting over an area is that the A-Train takes a snapshot of the clouds while ARM is able to observe the progression of the clouds as they move over the observing site.

Another difference between the ARM and A-Train instruments is that the ARM sensors have greater horizontal and vertical resolution. The lower horizontal resolution of the A-train instruments, such as 1 km for MODIS and similar resolution of the CPR, mean that if a pixel from MODIS (for example) is not overcast with clouds, then the cloud-free and cloudy areas within the pixel will be averaged and the instrument will observe lower intensities than the cloudy areas actually contain. This process is referred to as partial beam filling. The end result for this study is that the A-train instruments are most effective in areas of overcast cloud cover and will not be used in areas with low

cloud fractions.

Finally, the AMF suite of equipment includes a large range of sensors that provide a greater scope of remotely sensed and in-situ information than what is available from the A-Train constellation. The in-situ observations come from instruments such as radiosondes, the surface aerosol observing system, and surface meteorological instruments. Cloud dynamics information is gathered from the WACR Doppler measurements of Doppler velocity and Doppler spectral width, which are not available from the *Cloudsat* CPR. Additional equipment specific to the AMF suite include the micropulse lidar, ceilometer, and total sky imager, which provide valuable cloud and precipitation information.

CHAPTER 3

METHODS

K-Means Cluster

The K-means cluster is utilized in this study in order to objectively determine the cloud regime. It is assumed that the cloud regime is a product of dynamics and thermodynamics and that the dynamics of different meteorological environments differ and therefore produce unique cloud regimes. To test this, a combination of local thermodynamic and cloud macrophysical parameters from the CAP-MBL program are used to diagnose cloud regimes. This approach has three primary purposes. First is to gain further understanding about the overall state of MBL clouds in this region by analyzing the thermodynamics and macrophysics of these cloud regimes. Second is to explore the degree to which the dynamics are unique to, and ultimately coupled with, the objectively determined cloud regime. Third is to identify representative case studies within the resulting cloud regime and study the microphysical cloud properties of that regime in more detail. Differences in these cloud properties are known to lead to differences in precipitation and absorbed solar radiation and therefore must be quantified.

The K-means cluster algorithm as outlined by Wilks (2006) is an ideal method for categorizing different cloud regimes using a suite of observable variables that will be described shortly. The basic idea of the cluster algorithm is to group together similar

values of a vector of several variables within one cluster, while assigning different values of the vector of several variables to other clusters. This allows for the similarity of individual cloud events to be maximized within clusters, while the similarity of cloud events is minimized between different clusters (Berry and Mace 2012).

The K-means cluster is the most commonly used nonhierarchical clustering method. Nonhierarchical clustering is more advantageous because it allows for the reassignment of observations into different clusters as the analysis occurs. The K-means approach starts with a random selection of values from the dataset and uses them to define the centroids or means for a prescribed number of clusters. Each event is then randomly assigned to one of the clusters. The approach continues and equation 1 is used in order to define the weighted Euclidean distance, *d*, between an individual event and the cluster centroid. Here, *i* represents the variable to be clustered, *j* indicates the vector element to be clustered, and *k* is the specific cluster. In addition, $\bar{x}$ represents the mean of the variables already clustered, and *x* represents the individual value. For this study, $w_i = 1/s^2$, where s^2 is the variance. In this form, equation 1 is known as the Karl-Pearson (K-P) distance and accounts for differences in the variance of each of six variables used in the cluster analysis (Wilks 2006).

$$d_{k,j} = \left[\sum w_i \left(\bar{x}_{k,j} - x_{j,i}\right)^2\right]^{1/2} \quad (1)$$

If *x* is in a cluster where d is minimized after equation 1 is performed, it will remain there. If not, *x* is reassigned to the cluster where its value is closest to the centroid and the cluster mean is recalculated. Once all the data have been sorted, the algorithm repeats itself by reassigning variables and recalculating the means. This repetition continues for a set number of iterations. If no reassignment of variables takes place and cluster means

are not changing as iterations continue, then the algorithm has converged and the goal of the K-means clustering has been reached. For this study, eight iterations are needed in order to attain convergence. Since the initial seeds are random, the entire cluster algorithm is run two to three times at the set number of iterations to ensure the same end result of centroid means is achieved.

One of the limitations of the K-means cluster is that the number of clusters must be predefined. The methodology when choosing the number of clusters is to get the largest number of unique centroid values. If centroid values between some of the clusters are very similar, then the number of predetermined clusters should be reduced. The method of Rossow et al. (2005) is adapted for use in this study in order to more objectively select the number of clusters. This method uses the following criteria: 1) the centroid mean values should not change significantly for different initial seeds, 2) the centroid means should differ significantly from each other, and 3) the distances between cluster centroids should be larger than member distances within the cluster. For a preset cluster number of less than six, the centroid mean values would change for different initial seeds. For both six and seven clusters, all three criteria were met. The advantage for six clusters was that the centroid means varied more from each other than for seven clusters. The advantage for seven clusters was that one of the clusters split into a precipitating and weakly precipitating regime. While little improvement was seen from six to seven clusters regarding the average distance within the cluster, the emergence of this new cluster provided unique cloud information. Eight clusters resulted in the clusters being too similar and criteria three not being met. Therefore, the ideal number of clusters for this study is seven.

In addition to defining different cloud regimes, the results of the K-means cluster give valuable information about these different cloud types. This information comes from the mean values of the six input variables, which are described in the following section and encompass the average thermodynamic environment, frequency of occurrence, amount of liquid water, precipitation, and heights.

Six Cluster Input Variables

Unless otherwise specified, the values used for the cluster analysis were calculated by computing the hourly mean of each input variable. If an equipment outage occurred or specified criteria (mentioned later) for any one variable were not met for a given hour, then none of the variables were used for that hour in the cluster analysis. In total, 8123 hours or roughly 59% of the possible hours from June 2009 to December 2010 were used in the cluster analysis. Of the 41% not used, 14% were during major equipment outages. The remaining 27% occurred either during minor equipment outages (lasting from 1-6 hours) or when hourly mean criteria for the six input variables, such as cloud fraction less than 10%, were not met.

Modified Lower Tropospheric Stability

The first input variable is a modified version of lower tropospheric stability (LTS). Normally, LTS is defined as the potential temperature at 700 hPa (θ_{700}) minus the potential temperature at 1000 hPa (θ_{1000}) with θ_{SFC} also common. The LTS has been used extensively in studies that focus on MBL clouds in areas impacted by a subsidence inversion (Wood and Bretherton 2006; Kubar et al. 2009). Here, the traditional LTS is modified in order to focus on the static stability beneath the base of the subsidence

inversion and remove the inherent stability that is always present within the inversion. θ_{900} was chosen to replace θ_{700} in order for the top level of the metric to most often be within the MBL, where the focus clouds of this study are located. Hereafter, this modified LTS of $\theta_{900} - \theta_{1000}$ will be referred to as the LTS-900. The LTS-900 hourly means were calculated using the radiosonde temperature profile with the closest time stamp. Due to the 6-hour frequency of radiosonde launches, the hourly mean LTS-900 values used for the cluster analysis remained the same for 6-hour increments.

Midtropospheric Stability (MTS)

This variable was used in order to quantify the stability of the midtroposphere. While MBL clouds do not reside in the midtroposphere, strong subsidence that extends into the midtroposphere has been shown to impact low clouds (Myers and Norris 2013). The Midtropospheric Stability (MTS) is defined here as $\theta_{500} - \theta_{700}$. Mitas and Clement (2006) used the range of θ_{500} to θ_{850} to look at stability in the midtroposphere but here, θ_{700} is selected in place of θ_{850} in order to remain above the base of the inversion. As with the LTS-900, temperature data from the nearest radiosonde launch time were used for this calculation, causing hourly means to be the same for each 6-hour increment.

Column-summed dBZ

dBZ values are observed using the WACR and represent the backscattered electromagnetic (EM) radiation from a specified volume. Within the limitation of Rayleigh theory, this EM radiation is proportional to the sixth moment of the size distribution in the specified volume and is most often associated with precipitation mode of droplets within a volume when they are present (Stephens 1994). Doppler velocity

and Doppler spectral width products from the WACR were not used in the cluster analysis. Column-summed dBZ values were used as opposed to column-maximum values for the purpose of describing the vertical extent and magnitude of precipitation. In order to calculate the hourly mean dBZ values, dBZ values were first converted from the logarithmic dB scale into reflectivity (Z) values. The in-cloud Z values for each vertical bin with a radar profile were then summed. Noncloud Z values were determined by a corresponding signal-to-noise ratio of less than -10 dB (Clothiaux et al. 1995) and were not included in the summation. Z returns above the freezing level (determined via temperature data from the nearest radiosonde time) and Z values while the radar was in cross-polarization mode were also not included in the summation. Operation in cross-polarization mode only occurred in 2009 as the radar operated in co-polarization mode exclusively in 2010. Once each profile was summed, the mean of the summed profiles was computed for each hour and converted to back to the logarithmic dBZ scale.

First Cloud Base Height (FCBH)

FCBH is intended to give the lowest cloud base and was measured using the ceilometer. Given the limitations of the ceilometer when multiple or thick clouds are present, only this lowest measurement was used. Since taking the mean might often result in a cloud height that was very different from observed values, the hourly mode was used for FCBH instead of the mean. Only values when a cloud base was detected are included in the hourly FCBH mode. In addition, FCBH values that were above the freezing level were not used in calculating the mode for the hour.

Cloud Fraction

FCBH data from the ceilometer were used to calculate the cloud fraction. The cloud fraction is the ratio of ceilometer observations where a cloud base was detected below the freezing level to total number of ceilometer observations during each hour. This is often referred to as temporal cloud fraction as opposed to area cloud fraction, or the amount of an area covered in clouds at any given time. Temporal and area cloud fraction have been compared and assumed to be commensurate in the past (e.g., Brooks et al. 2005) but only temporal coverage was computed for this study. Again, clouds detected above the freezing level were not included in determining the cloud fraction. If the cloud fraction was less than 10%, then that hour was not included in the cluster analysis (REM12).

LWP

LWP was the final variable used in the cluster analysis and is derived directly from the MWR. LWP is the vertical integration of column LWC or the total amount of liquid water available to fall as warm rain (Sorooshian et al. 2010). See Liljegren (1994) for a detailed description of the calculation of LWP from passively sensed microwave energy. As there is no way to remove the contribution of any super-cooled liquid water above the freezing level, MWR measured LWP values may contain super cooled water. Values flagged by the MWR as "wet window" are not used to calculate the hourly mean LWP. Also, if more than 90% of an hour had this flag present, that hour was not included in the cluster analysis. LWP values greater than 2000 g m^{-2} while the window was reportedly dry were not included in the hourly mean as these values were deemed to be too large to have occurred unless precipitation was reaching the window and are

assumed to be times when the wet window flag was not functioning properly. Using this methodology for the entire 19-month CAP-MBL campaign, the wet window flag did not function properly 0.49% of the time. This was equal to approximately 8,775 of 1,797,348 observations.

New Microphysical Retrieval Algorithm

Evidence strongly suggests that precipitation is ubiquitous within MBL clouds whether or not that precipitation is actually reaching the surface (Fox and Illingworth 1997; Snodgrass et al. 2009). Figure 2 displays that a large or precipitation sized mode was evident during the RICO and MASE field campaigns. Further field campaign evidence occurred during CAP-MBL, as Kollias et al. (2011) showed the ubiquity of drizzle in Azores marine Sc by indicating that drizzle particles exist in maritime clouds at very low reflectivities. In addition, the WACR detected dBZ echoes below half of all ceilometer indicated cloud bases at GRW during CAP-MBL (REM12). Recent campaign work shows that Sc precipitate much more than was previously thought (Wood 2012). Knowing that cloud droplets are also always present as displayed in the smaller size mode of Figure 2, there is an obvious necessity to represent both cloud and precipitation sized hydrometeors within the PSD. Indeed the most pressing questions regarding MBL clouds have to do with the processes that result in cloud water evolving into precipitation in the presence of varying aerosol backgrounds and dynamical forcing. Assuming a correct PSD shape is critical to the accurate retrieval of cloud microphysical parameters such as r_e, N_d, and precipitation rate (R) (Mace 2010). A single mode PSD implies that a certain volume with hydrometeors is populated by either cloud or precipitation-sized droplets. Most retrieval algorithms make a single mode assumption

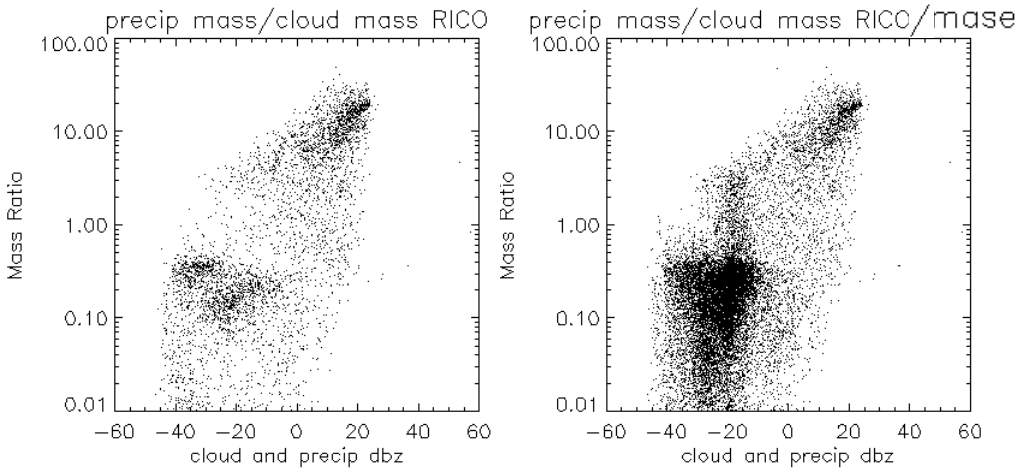

Figure 2. Hydrometeor droplet mass ratio vs. cloud and precipitation dBZ. The plot on the left is for the RICO field campaign and the plot on the right is combined for the RICO and MASE field campaigns.

and are thereby limited to deriving PSD properties of either mode or some combination of the modes that is difficult to interpret. Zhao et al. (2011) show that a bimodal PSD can improve the accuracy of retrieved cloud microphysics when compared to a single mode PSD. Utilizing a bimodal PSD that simultaneously gathers the properties of cloud and precipitation modes is an important aspect of this algorithm.

A second key aspect is the synergistic utilization of different sensors in order to provide a maximum amount of information regarding cloud and precipitation sized hydrometeors within a profile. Two separate but similar instrument compliments are used to achieve this goal. The first set of equipment comes from the ground-based ARM CAP-MBL field campaign. In CAP-MBL, the input variables come primarily from three independent surface-based remote sensors. First is the WACR, which is most sensitive to the largest hydrometeors within a given resolution volume due to the dependence of Z on the sixth moment of hydrometeor PSD. This means that when precipitation-sized hydrometeors are present, the WACR will primarily respond to the precipitation mode. However, when the cloud mode is dominant, the WACR gathers information about the cloud mode as the majority of the largest hydrometeor sizes will be in the cloud mode. Second is a microwave radiometer that records downwelling radiation in the 23 and 31 GHz bands that provide information on column liquid water and ultimately gives cloud mode information with a typically smaller contribution from precipitation size drops. The exception to this is when precipitation dominates the fraction of condensed mass (Figure 2). Third is the SKYRAD, which is used to measure visible and IR radiant fluxes from clouds. Visible radiant fluxes provide information about cloud properties while the near IR contributes some information regarding precipitation properties (Nakajima and

King 1990). Broadband solar flux has been used in many studies to retrieve cloud properties in MBL clouds (e.g., Dong and Mace 2003). Additional and important cloud and column information is gathered from radiosonde launches and a laser ceilometer.

The satellite-borne instruments within the NASA A-Train constellation record a similar set of synergistic measurements. Radar reflectivity from the cloud profiling radar (CPR) on *Cloudsat* is similar to the WACR. The CPR is most sensitive to precipitation-sized hydrometeors, but otherwise gathers information about cloud particles when they predominate within a resolution volume. The CPR is also used to derive a new measurement that contains information about the amount of liquid water within the profile. This new measurement has been developed by Dr. Simone Tanelli and collaborators at the NASA Jet Propulsion Lab and is similar to what would be observed using a passive microwave radiometer operating at the *CloudSat* frequency of 94 GHz. The idea for this 94 GHz radiometric measurement developed when it was noticed early on in the *CloudSat* mission that the noise floor of the radar seemed to rise and fall as the satellite passed over liquid-phase clouds. This modulation of the noise floor, it was realized, was due to microwave emission from these clouds. Tanelli et al. calibrated this noise variation against calibrated 89 GHz measurements from the AMSR-E radiometer on the Aqua satellite so that a microwave brightness temperature or T_b was derived. The advantage of the CPR 94 GHz T_b measurement is that since it is derived from a signal within the CPR noise, it gives critical cloud liquid water information for the same footprint as the CPR (Tanelli, personal communication). While the uncertainty in the *Cloudsat* 94 GHz T_b measurement is approximately twice what is achieved from an actual radiometer like AMSR-E, the footprint coincidence is a major advantage over

AMSR-E, which has a footprint of approximately 10 km. Like measurements from the MWR, the 94 GHz T_b measurement mostly gives information on the cloud properties but precipitation mode particles also contribute when they are present in significant amount.

The third measurement comprises solar reflectances in narrow spectral bands at 0.55, 1.6 (both cloud properties), and 2.1 micrometer wavelengths providing information regarding cloud and precipitation properties from the MODIS instrument. Nearly 95% of the MODIS signal comes from cloud mode sized particles (Lebsock et al. 2011). In summation, due to the near ubiquity of precipitation in MBL clouds, cloud radar predominately senses precipitation mode properties while SKYRAD and MODIS sense information from the cloud droplet mode, and an algorithm that exploits a combination of these instruments must assume a bimodal PSD in order to be successful.

The tangled information from either the ground or satellite based measurements is inverted within an optimal estimation framework using prior data from the RICO and MASE campaigns along with a first guess profile. The first guess starts with an assumption of what fraction of the LWP (from either the MWR or CPR 94 GHz T_b measurements) is due to cloud and what fraction is due to precipitation using an innovative study by Lebsock et al. (2011). Solar flux transmittance and either the 31 GHz MWR or 94 GHz CPR T_b are used to estimate a column-average modified gamma PSD in order to calculate a column N_d. An assumption is made that this column N_d is applicable from cloud base to cloud top (Miles et al. 2000). An initial estimate of the liquid water content profile is then derived using the Frisch et al. (1998) approach of distributing the LWP vertically using a radar reflectivity (Z) to the ½ power weighting, hereafter LWC_F. The estimated vertical profile (LWC_E) is assumed to follow an

adiabatic shape from cloud base to cloud top. N_d and LWC_E are used to derive a profile of modified gamma PSDs that satisfy these estimates. Z is also estimated within the first guess (Z_{est}) and is compared to the observed Z (Z_{obs}). This comparison is used to redistribute the LWC_E by taking water from LWC_E where $Z_{est} > Z_{obs}$ to where $LWC_E < LWC_F$, until $Z_{est} \leq Z_{obs}$. This process is repeated until $Z_{obs} \geq Z_{est}$. Where $Z_{obs} > Z_{est}$ in the cloud and below the ceilometer-measured cloud base, it is assumed that precipitation is present and a second modified gamma distribution is derived consistent with $Z_{obs} - Z_{est}$ and the fraction of the observed LWP that is taken to be from precipitation following Lebsock et al. (2011). The end result is a profile of microphysics that when passed through appropriate radiative transfer models is able to reasonably reproduce the measured solar flux or solar reflectance, the microwave T_b, and the radar *Z* profile.

Three radiative transfer forward models are also used as part of the retrieval algorithm. The first is a radar forward model using Mie backscatter and extinction along with a direct integration of modified gamma PSDs (Posselt and Mace 2014). SKYRAD or MODIS reflectances are forward modeled using a Radiant 2.0 eigenmatrix solver (Christi and Gabriel 2003) and microwave information is modeled in the same way as Kummerow et al. (1996) with modification and improvements as described by Lebsock et al. (2011). The cloud microphysical outputs from this algorithm are probability distribution functions of both the cloud and precipitation phases of variables such as N_d, r_e, and LWC along with R and τ for the column. Vertical velocity (W) is also retrieved when using the ground-based ARM equipment.

Both the ARM and A-Train based retrieval algorithms use exactly the same methodology and nearly the same computer code. The differences in the ARM and A-

Train versions come from differences in the satellite or ground-based measurements, specifically the LWP. The retrieval algorithm is configured in this study to only look at the liquid phase and is thus limited to clouds below the freezing level. Another limitation of the retrieval algorithm is that only a single layer of clouds may be present. Additional cloud layers also contribute to what is observed by the visible and IR sensors, causing contamination of the signal if multiple cloud layers are present. Finally, the algorithm only works during the day as visible radiant fluxes (either from SKYRAD or MODIS) are used to retrieve information about cloud mode hydrometeors.

CHAPTER 4

RESULTS

Cluster Regimes

The K-means cluster algorithm produces the ideal amount of information when run with seven clusters. The cluster output data are subjectively analyzed in a number of ways in order to compare and contrast each cluster and determine the type of cloud each cluster predominately represents. These seven clusters represent the spectrum of warm clouds that occurred over the observing site during the 19-month CAP-MBL campaign. These seven cloud regimes vary in the means of the six observed cloud and thermodynamic properties that were input into the cluster algorithm. Figure 3 shows the mean and standard deviation for each of the six input variables for all seven clusters. While seven unique cloud regimes are indicated, these regimes are further grouped into three broad categories that are illustrated by the different color shades. These broad categories first include the most common MBL clouds of weakly precipitating and precipitating Sc, Cu and St (shown in red), fair weather Cu (shown in blue), and finally deep MBL clouds (shown in green). While a detailed discussion of the differences between individual regimes and the broader categories will be the focus of the next section, certain trends of the broad categories are shown in Figure 3. For example, the precipitating Sc, Cu, St are distinguished by mean values of > 0.7 cloud fraction, > 50 g m^{-2} LWP, and > -20 dBZ. The fair weather Cu are distinguished by lower mean values

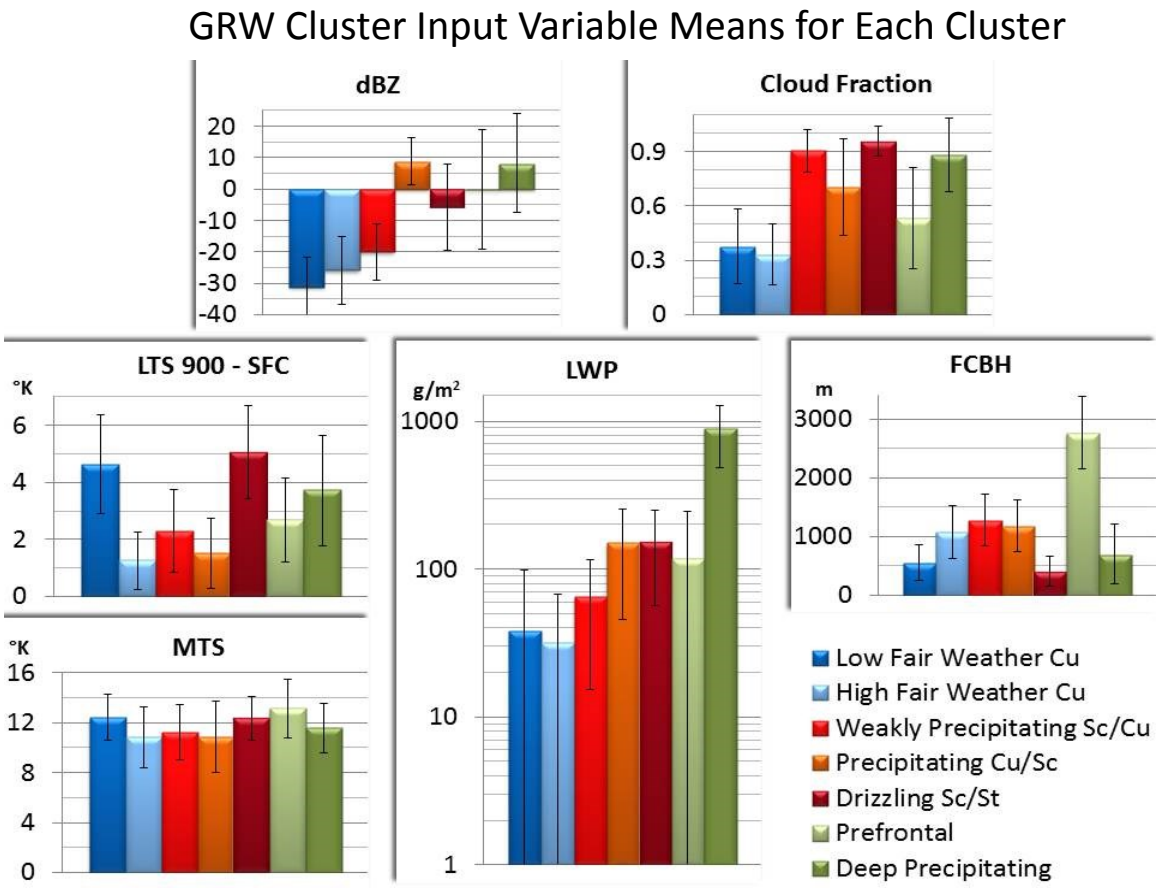

Figure 3. Mean and standard deviation grouped by cluster input variable for each of the seven cloud regimes (clusters). Legend for the cloud regimes is located in the bottom right. Note the use of log plot in the bottom center for the LWP variable.

with cloud fractions < 0.4, LWP < 50 g/m^2, and dBZ values < -20 dBZ. The most notable characteristics of the deep MBL clouds are the very high LWP and FCBH outlier values along with positive dBZ values. Multiple studies (e.g., Wood and Bretherton 2006; Zhang et al. 2010) have previously shown a positive correlation between increases in traditional LTS and low cloud fraction to include during the CAP-MBL project (REM12). This occurs as increased LTS causes warm moist air to be trapped in the MBL. Does the same correlation exist between LTS-900 and cloud fraction for the cluster means? Figure 3 shows some positive correlation between LTS-900 and cloud fraction for means of the drizzling Sc/St and high fair weather Cu cloud regimes. However, the opposite is true for low fair weather Cu and weakly precipitating Sc/Cu as these two regimes show a negative correlation. This combines into an overall LTS-900 and cloud fraction correlation coefficient of 0.30 for all clusters. In contrast, if the two negatively correlated clusters are removed from the correlation calculation, the coefficient increases to 0.56. While this result is interesting, there is no obvious connection between the low fair weather Cu and weakly precipitating Sc/Cu clusters and no glaring difference between these two clusters and the rest. One possible explanation for this lack of correlation between LTS-900 and cloud fraction is that by design, the LTS-900 is too shallow to include the base of the subsidence inversion and should not be compared to LTS, which does include the inversion base. Perhaps what is occurring is the θ_{900} value of LTS-900 is actually more correlated with cloud thickness than cloud fraction and that this correlation with cloud thickness is negative. This might be because areas dominated by a subsidence inversion generally observe a thermodynamic jump at cloud top, which also coincides with the base of the subsidence inversion (Gerber et al.

2013). It is possible that when cloud bases and tops are low, the thermodynamic jump will occur below 900 hPa and LTS-900 will be higher for low clouds than for higher clouds.

To test the thermodynamic jump, the correlation coefficient for the cluster means of LTS-900 and FCBH is computed as -0.48, which is .18 higher than for LTS-900 and cloud fraction. If the prefrontal cluster is removed from this calculation, the correlation between LTS-900 and FCBH jumps to -0.93. Removal of the prefrontal cluster mean FCBH of 2765 m is appropriate given that the subsidence inversion is not present during this cluster. This cluster was also very infrequent and represents only 4% of the total occurrences. Therefore, focusing only on regimes when the inversion is present, cloud base is more negatively correlated with LTS-900 than cloud fraction is positively correlated with LTS-900. Thus, LTS-900 values are more likely to be connected to the level of the clouds than the true instability of the surface up to the 900 hPa level. Calculations for cloud top height were not included in this study but it is likely that cloud top would be even more negatively correlated with LTS-900 than is cloud base.

Figure 4 shows histograms of monthly occurrence and the overall percentage of occurrence for each cluster for the 19-month campaign. The mean number of occurrences for months 6-8, 10, and 11 are used since both 2009 and 2010 data were available for those months. Months 1-5, 9, and 12 only had 1 year of data owing to the length of the campaign, WACR outages in September 2010, and no radiosonde launches from early December 2009 to early January 2010. Since the majority of months only have one year as their sample size, Figure 4 does not represent a climatological occurrence of the clusters but is meant as a starting point in determining the time of year

when each cluster tends to occur. This is also helpful in determining which cloud regime each cluster resembles, as the monthly cluster occurrence can be compared to other CAP-MBL studies that give low cloud climatology. The weakly precipitating Sc/Cu regime in Figure 4 shows a maximum from midsummer through early fall and occur fairly often. Precipitating Cu/Sc are opposite with a winter max and summer minimum. Drizzling Sc/St clouds are at a maximum in the summer and the two fair weather Cu clusters are more uniform with maxima in the spring and fall. The seasonality of these five regimes coincides well with results from REM12. Deep MBL clouds include prefrontal, which peak during the transition seasons and coincide with the maximum of synoptic scale disturbances, and deep precipitating which peak during the winter with synoptic systems and occasionally during the summer due to deep convection. Of note is the convective and infrequent nature of these two deep clusters, each occurring only 4% of the total cluster hours.

In addition to the information in Figures 3 and 4, each cluster's average synoptic scale meteorological environment and each cluster's average dBZ contoured frequency by altitude diagram (CFAD) are also computed (to be shown later with specific cluster results) to aid the subjective regime analysis. The average meteorological environment is represented using the National Centers for Environmental Prediction–National Center for Atmospheric Research (NCEP–NCAR) reanalysis data (Kistler et al. 2001). Since the reanalysis data are only available every 6 hours at 00, 06, 12, and 18 UTC, the nearest reanalysis hour to each cluster hour is selected and then averaged for each cluster to create the meteorological environment in a four-panel composite. Because of the lower temporal resolution of the reanalysis data, the corresponding reanalysis synoptic regime

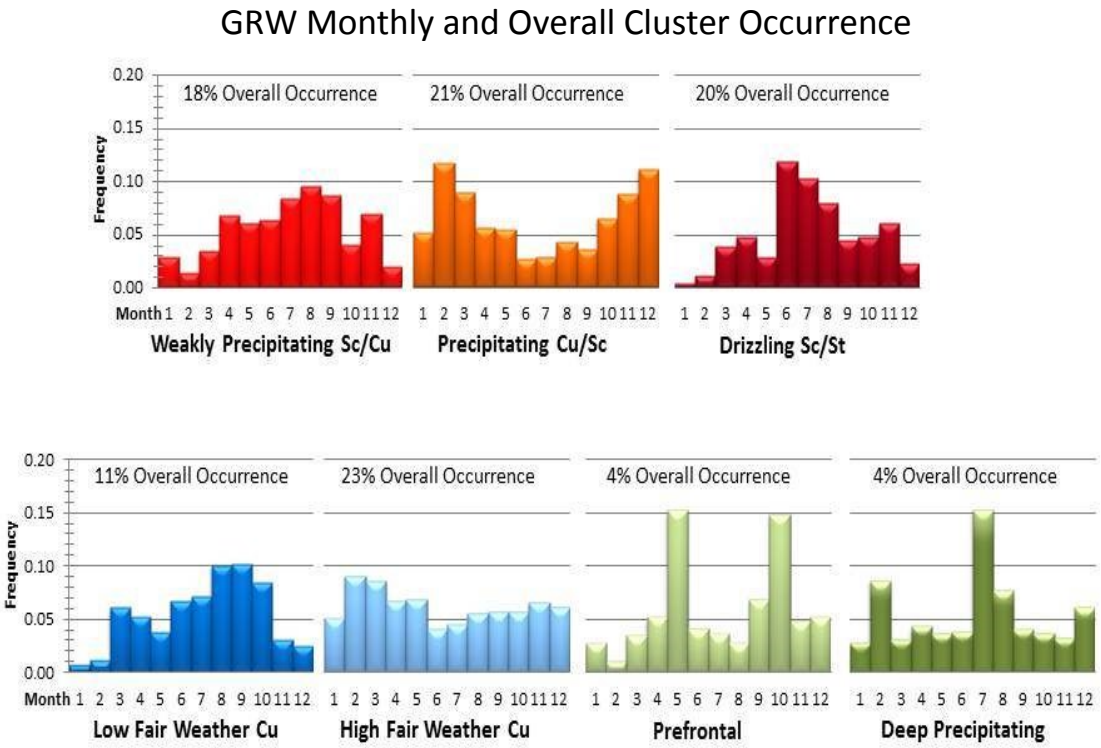

Figure 4. Histograms of monthly and overall occurrence by cluster. The top row (red) are the weakly precipitating and precipitating Sc, Ct and St clusters. The bottom row from left to right are the two fair weather Cu clusters (blue) and deep MBL clusters (green).

might differ from the actual cluster hour synoptic regime. The averaging of all reanalysis hours for each cluster should minimize this difference and still provide some useful synoptic information and trends. The four-panel composite features geopotential heights and winds at 300, 500, 850, and 1000 mb. Also included in the composite are 850 mb temperature contours, surface sensible net heat flux, and both 850 and 500 mb vertical motion.

CFAD diagrams (shown with cluster results) display the frequency, or in this case occurrence, of a variable with height (Yuter and Houze 1995). In this study, CFADs include raw WACR reflectivity and raw WACR Mean Doppler Velocity (MDV) from the surface to 5 km. Therefore, MDV is a measure of the velocity of the hydrometeors detected by the WACR. The height of 5 km was chosen in order to focus on radar information below the freezing level and at temperatures higher than 0 degrees C. The CFADs are created by counting reflectivity occurrences for a specified reflectivity and height range or specified volume. This count is then normalized by the total counts across all possible volumes and the normalized values are multiplied by 100 in order to reduce significant Figures. Signal to noise values below -10 dB were not included in the CFAD histograms.

Group 1 – Neutral Sc, Cu, and St

This group comprises the three clusters of weakly precipitating Sc/Cu, precipitating Cu/Sc, and drizzling Sc/St. One reason these clusters are grouped together and labeled “neutral” is that they are all dominated by weak synoptic forcing with near neutral vertical motion at 500 and 850 mb. They are also categorized together based on their cluster means, having relatively high cloud fractions, LWP values, and dBZ values

and each occurs roughly 20% of the time in Figure 4. Combining this high level of occurrence with the high cloud fraction means these three cloud regimes are the most prevalent MBL clouds and have the greatest impact on the earth's radiation budget over the North Atlantic. Given the results of Tseioudis (2014) where the Azores act as a proxy for global clouds, the prevalence and radiation impact of these cloud regimes could be applied globally as well, which is a profound result.

The first cluster of this group is the weakly precipitating Sc/Cu. Figure 3 indicates that this cluster is characterized by the third lowest dBZ and LWP cluster means along with the second highest cloud fraction of approximately 90%. Figure 5.a shows nearly zonal flow at 300 mb along with neutral vertical motion at 500 and 850 mb. Weak ridging and high pressure are evident from the mid- to low levels with a closed high at the surface. The most pronounced (but weak) warm air advection of any cluster occurs at 850 mb and might help create an environment with higher than average FCBHs. The CFAD in Figure 5.b shows a concentration of weak dBZ echoes with dBZ values rarely exceeding 2 km, equating to average cloud thickness less than 1 km. MDV values are predominately positive and concentrated around 0.15 m s^{-1}. Positive values are toward the radar or in the downward direction. This cluster is most common during the summer time and its monthly occurrence peaks match up well with the peak occurrence of the Sc and the Cu under a Sc cover (Cu + Sc) cloud types from REM12. The Cu + Sc occur within a decoupled boundary layer with Cu bases forming at the base of the transition layer and the Sc tops reaching the subsidence inversion base (Krueger et al. 1995; Yin and Albrecht 2000). A relatively deep MBL allows for this multilayer cloud formation and this cluster's relatively high FCBH indicates a slightly deeper MBL. Due to these

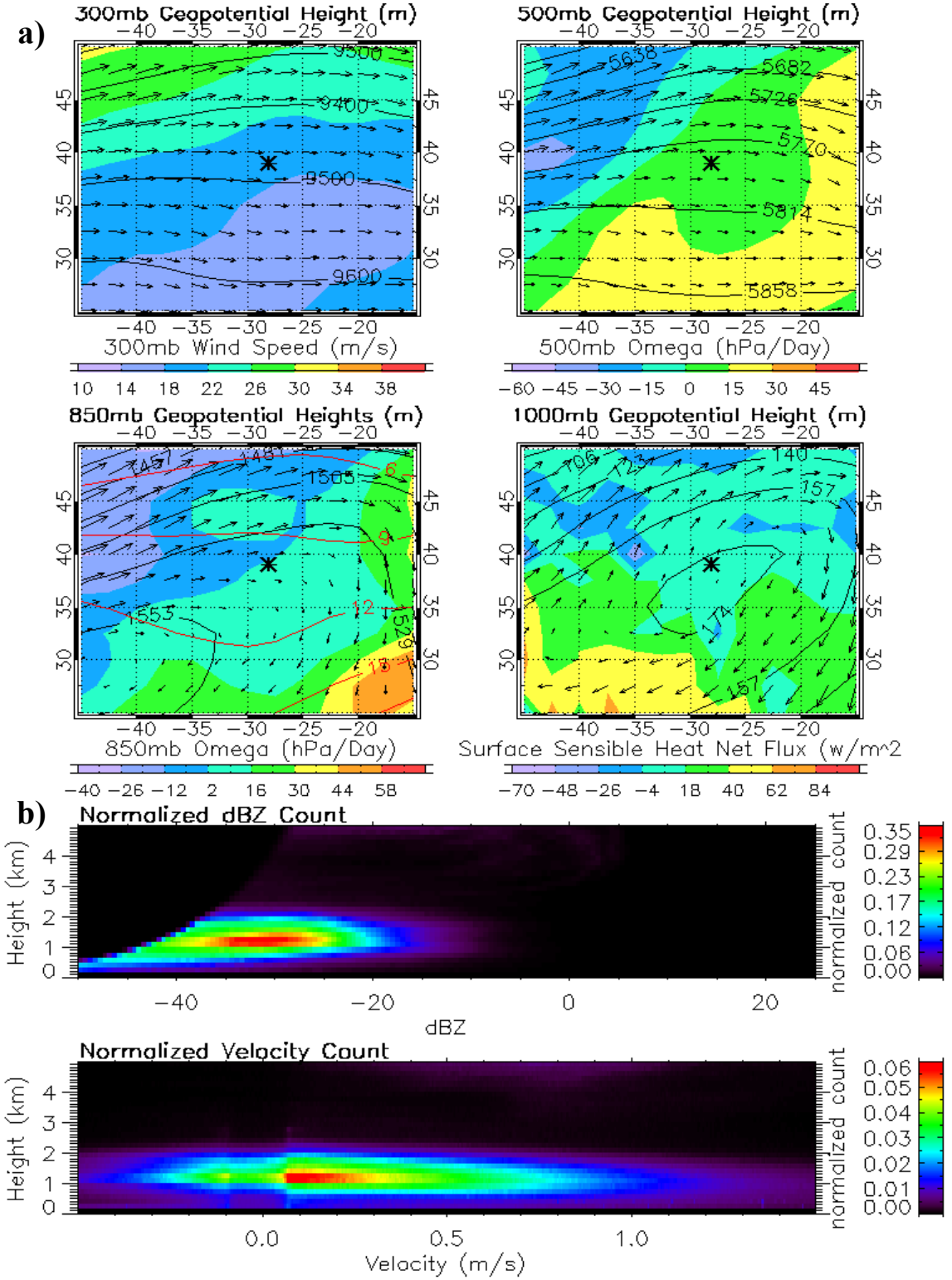

Figure 5. Weakly precipitating Sc/Cu cluster. (a) NCEP/NCAR Reanalysis, the asterisk marks GRW. All black contours show heights at the respective pressure levels with a red contour for temperautre at 850 mb (bottom left). Shading is wind speed (top left), Omega (top right and bottom left), and Surface Sensible Heat Flux (bottom right). (b) Normalized CFADs for reflectivity (top) and MDV (bottom). Positive MDV is downard.

factors, the Cu + Sc cloud occurrence should be common within this cluster.

The next cluster is the precipitating Cu/Sc and is depicted in Figure 6. The mean LTS-900, MTS, and FCBH values for this cluster are quite similar to, and easily within one standard deviation of, the weakly precipitating Sc/Cu values. The main difference between these two cloud regimes is the precipitation amount, with this regime having the highest average dBZ value of any cluster (see Figure 3). It also has a lower average cloud fraction than the weakly precipitating Sc/Cu and drizzling Sc/St, indicating more Cu and/or open-cell Sc within this cluster. Figure 6.a indicates fairly weak vertical motion in the midlevels, which is similar to the weakly precipitating Sc/Cu regime. This Figure also indicates troughing in the midlevels that should coincide with upward vertical motion, which is in contrast to the ridging of the weakly precipitating Sc/Cu. The most pronounced (but weak) cold air advection (CAA) is evident at 850 mb. CAA at this level would decrease MBL stability and may explain the higher Cu concentration in this cluster. Surface sensible heat flux shows slightly negative values, indicating that surface water is cooler than the overlying air, although this may seem counterintuitive with CAA. However, the surface water being colder would act to cool the boundary layer, which could result in high humidities and potentially increase the propensity for precipitation. Since this cluster is most common during the winter and transition seasons, it is likely that these clouds favor development in the relatively unstable postfrontal synoptic environment. During this synoptic situation, the semipermanent subtropical high is weaker and to the south, meaning a decrease in overall subsidence. Low values of LTS-900 and MTS give additional evidence to this theory. The weakened subsidence allows these MBL clouds to grow deeper (as seen in the CFAD of Figure 6.a) and for heavier

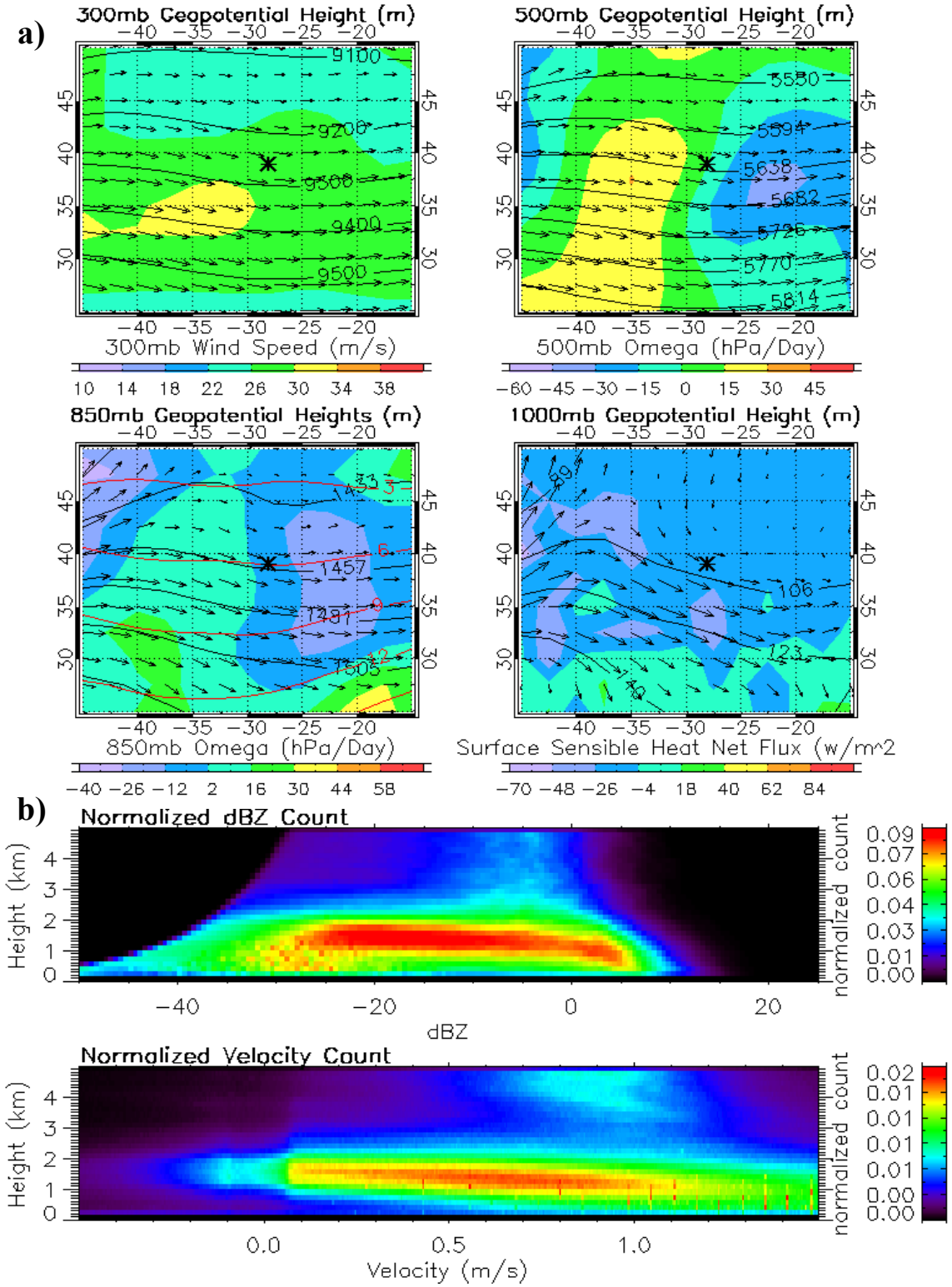

Figure 6. Precipitating Cu/Sc cluster. (a) NCEP/NCAR Reanalysis, the asterisk marks GRW. All black contours show heights at the respective pressure levels with a red contour for temperautre at 850 mb (bottom left). Shading is wind speed (top left), Omega (top right and bottom left), and Surface Sensible Heat Flux (bottom right). (b) Normalized CFADs for reflectivity (top) and MDV (bottom). Positive MDV is downard.

precipitation to form than in the weakly precipitating Sc/Cu cluster. Standard deviation bars from Figure 3 show some spread but more convincing is the CFAD from Figure 6.b, which indicates the most variability of any of the seven cloud clusters and adds some caution to the representativeness of the outliers within this cluster. MDV values vary greatly with the majority between 0 and 1 m s^{-1}. These are some of the highest values of any cluster and corroborate large, precipitating hydrometeors.

The third cloud cluster of this group is the drizzling Sc/St regime. This low cloud cluster has the lowest FCBH, smallest FCBH standard deviation, highest cloud fraction, and highest LTS-900 of any cluster. The highest LTS-900 and cloud fraction combine to give the positive correlation between low-level stability and amount of cloud cover. This gives additional evidence for a Sc/St regime as other studies have found the LTS and cloud fraction correlation to be most pronounced for Sc (Wood and Bretherton 2006; Zhang et al. 2010). This cluster also shows the aforementioned strong negative correlation between LTS-900 and FCBH with the highest average LTS-900 and lowest FCBH. Figure 7.b shows hydrometeor tops average below 1km, indicating relatively thin clouds as well. This regime is most common during the summer months and peaks during early summer. The capping effect of a strong subsidence inversion during summer creates a lower inversion base and enables the low cloud base, shallow cloud depth, and high cloud fraction of these clouds. This is documented by REM12 with the inversion base being lowest in early summer along with the highest Sc cloud fraction during this time. Figure 7.a shows the most pronounced ridging and highest near surface pressure of any frequently precipitating cluster. The frequently observed Cu + Sc are likely to also be common during this cluster because of the high cloud fraction and

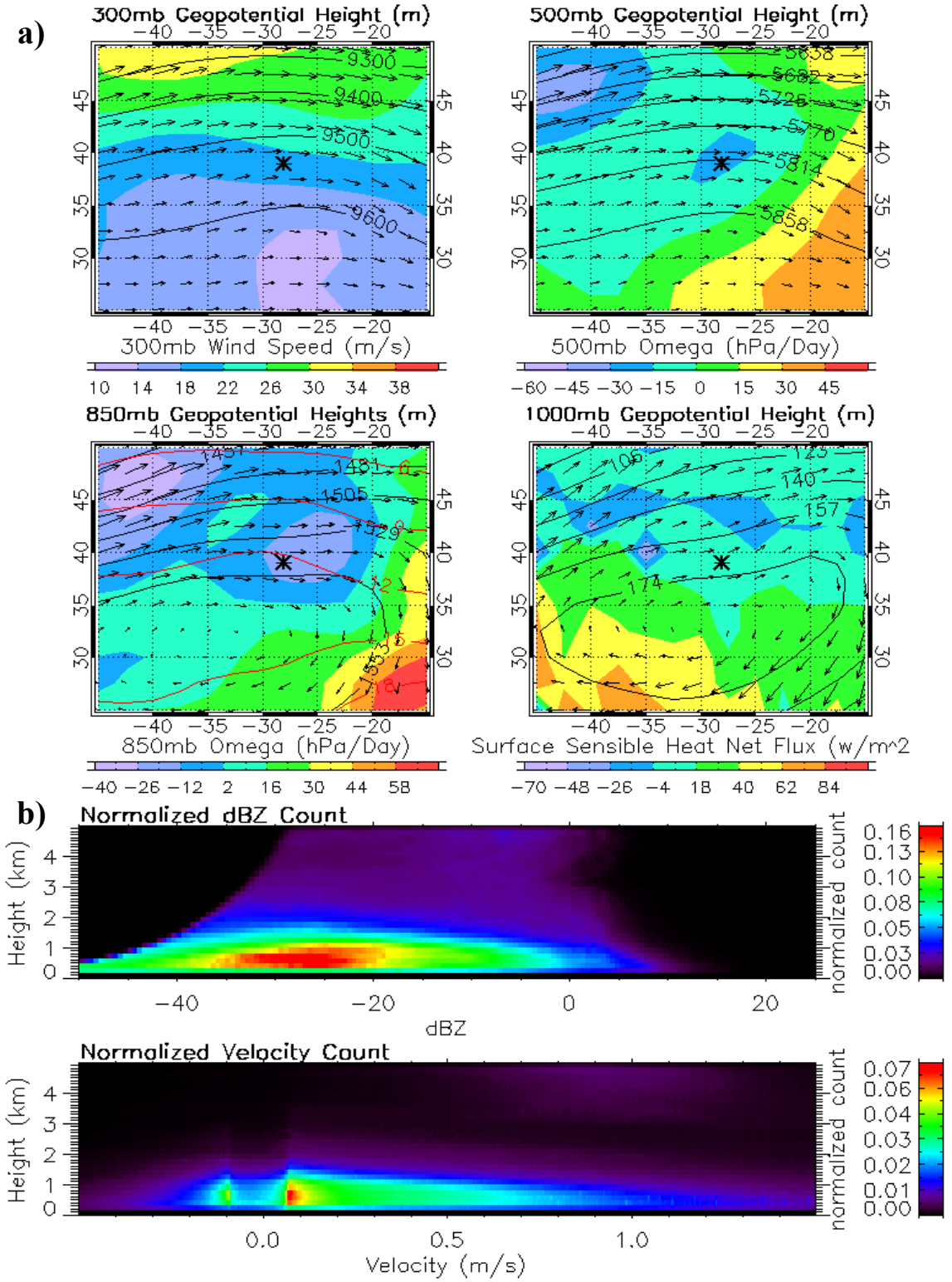

Figure 7. Drizzling Sc/St cluster. (a) NCEP/NCAR Reanalysis, the asterisk marks GRW. All black contours show heights at the respective pressure levels with a red contour for temperautre at 850 mb (bottom left). Shading is wind speed (top left), Omega (top right and bottom left), and Surface Sensible Heat Flux (bottom right). (b) Normalized CFADs for reflectivity (top) and MDV (bottom). Positive MDV is downard.

highest occurrence during the summer. This regime drizzles frequently with an average dBZ of -5.7 and approximately the same LWP as the precipitating Sc/Cu regime. MDV values are highly concentrated, which adds confirmation to the uniformity of the clouds that make up this regime.

Group 2 – Negatively Forced Fair Weather Cu

In contrast to other clusters that may include more than one cloud type, Cu dominates the two clusters of this group. They are defined by the lowest dBZ, cloud fraction, and LWP averages of any cluster. These low values correlate well with the most negative (downward) subjective vertical forcing in the mid- to low levels. Their combined average cloud fraction of just above 30% is close to the 25% trade wind Cu cloud fraction for the CAP-MBL campaign (Ghate et al. 2011). Both clusters have summer minimums and peaks in a transition season, matching Cu statistics by REM12. Together, they occur during 34% of the study period.

The first cluster in this group is the low fair weather Cu regime. It is categorized as the cluster with the weakest precipitation with the lowest average dBZ of -31.2. Figure 8.b shows the most negative dBZ distribution of any CFAD along with low values for MDV. The low MDV values are likely due to low cloud heights, as velocities tend to increase with height. Low MDV values could also mean smaller droplets, as smaller hydrometeors have lower velocities. These weak clouds are low and thin with the second lowest FCBH and low tops. Ghate et al. (2011) also found trade wind Cu in this region to also be relatively low and thin. Being associated with the trade wind environment coincides well with the summer time maximum of this cluster. Compared to the other very low cloud regime, the drizzling Sc/St, the low fair weather Cu regime appears to

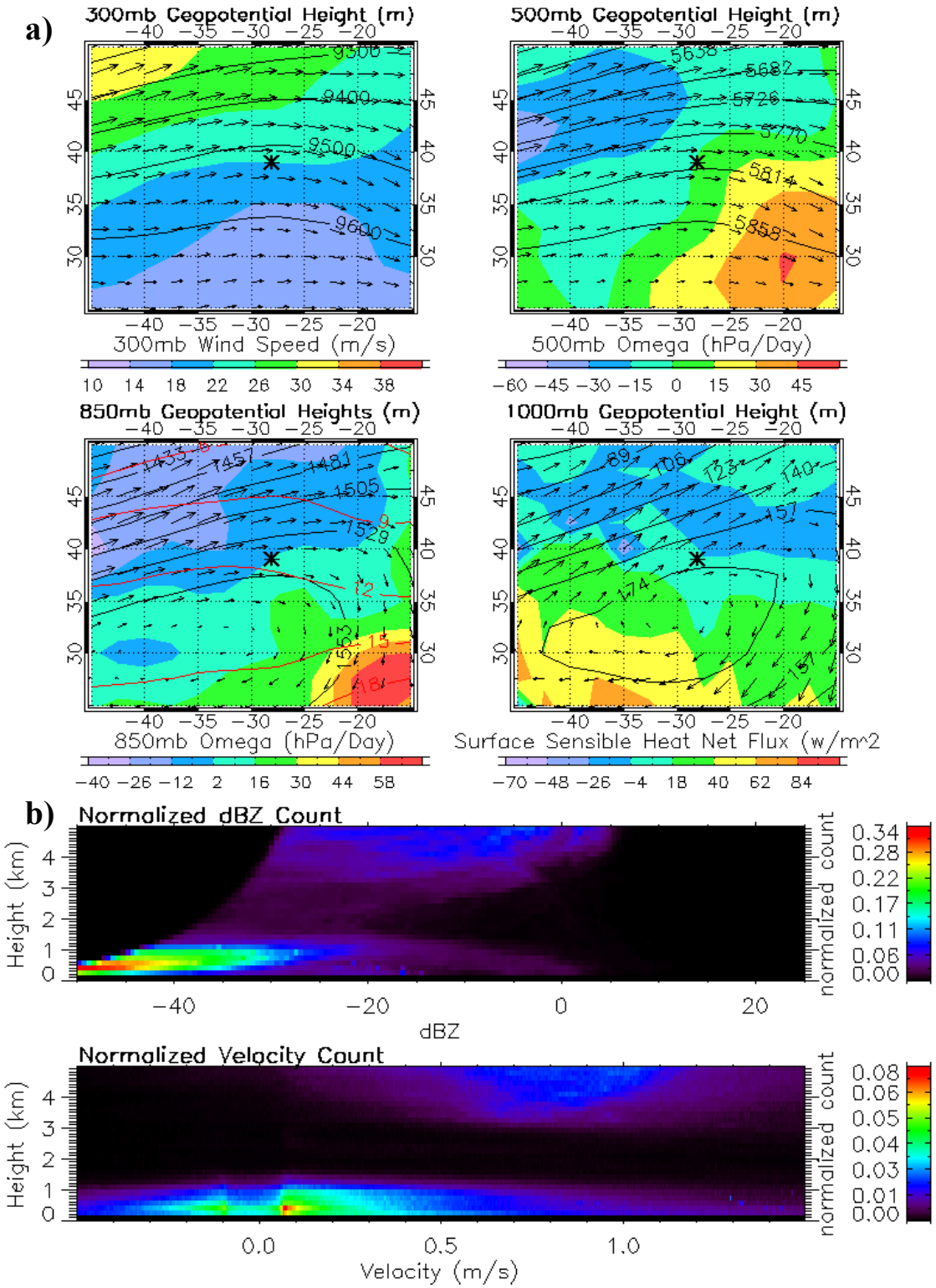

Figure 8. Low fair weather Cu cluster. (a) NCEP/NCAR Reanalysis, the asterisk marks GRW. All black contours show heights at the respective pressure levels with a red contour for temperautre at 850 mb (bottom left). Shading is wind speed (top left), Omega (top right and bottom left), and Surface Sensible Heat Flux (bottom right). (b) Normalized CFADs for reflectivity (top) and MDV (bottom). Positive MDV is downard.

have less height variation. This cluster shows the worst positive correlation between LTS-900 and cloud fraction and is the main reason the overall correlation between the two is so low. However, it is this cluster that gives additional evidence that LTS-900 is negatively correlated to FCBH owing to the second lowest FCBH and second highest LTS-900.

The next regime is the high fair weather Cu regime. As the name suggests, the primary difference between the two Cu regimes of this group is the FCBH with an average of 1175 m for this cluster and 556 m for the lower cluster. Another notable difference lies in the LTS-900 values, which are low for the high fair weather Cu clouds and high for the low fair weather Cu clouds. This is likely tied to the thermodynamic jump experienced at cloud top. Additional differences are evident in Figures 8.a and 9.a with downward motion at 500 mb and 850 mb being much stronger in this regime and the strongest of any cloud regime. While the strong descent does coincide well with the low dBZ, low cloud fraction, and low LWP values, it is perhaps counterintuitive that the high-based fair weather Cu regime would have stronger descent than the low-based fair weather Cu regime. Theoretically, the stronger descent would mean a much shallower MBL and a FCBH much closer to the ground, but that is not the case. The fact that these high fair weather Cu occur least frequently during the summer might provide an explanation for the discrepancy between FCBH and descent. Not occurring as much during summer allows for a deeper MBL and higher FCBH and the strong descent is likely the result of high-pressure systems in-between synoptic frontal passages. The synoptic four-panel in Figure 9.a confirms that the high-pressure systems of this cluster are shallower, which is representative of non-summer transitory highs. This regime also

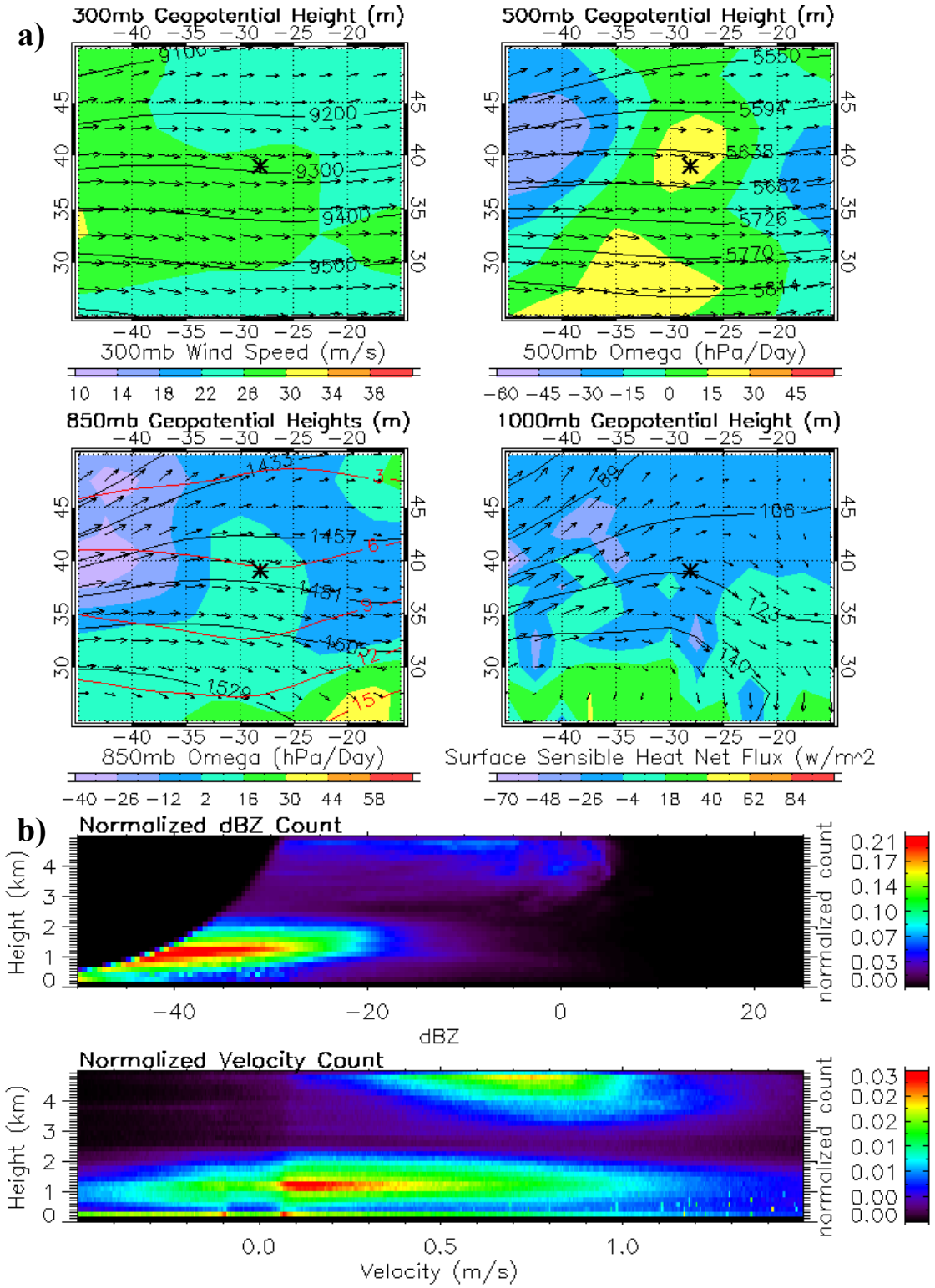

Figure 9. High fair weather Cu cluster. (a) NCEP/NCAR Reanalysis, the asterisk marks GRW. All black contours show heights at the respective pressure levels with a red contour for temperautre at 850 mb (bottom left). Shading is wind speed (top left), Omega (top right and bottom left), and Surface Sensible Heat Flux (bottom right). (b) Normalized CFADs for reflectivity (top) and MDV (bottom). Positive MDV is downard.

has a negative surface sensible heat flux, indicating the air near the surface is warmer than the underlying water. Figure 9.b shows much more variation among the dBZ and MDV values when compared to Figure 8.b and separated, higher MDV count values above 3 km indicate midlevel clouds also occur during this cloud regime. The dBZ CFAD also shows what appears to be an increasing trend in values with height, indicating larger drops near cloud top and few hydrometeors reaching precipitation sizes. These two Cu regimes are the only ones with this feature.

Group 3 – Positively Forced Deep MBL Clouds

The final two clusters are comprised of clouds that extend beyond the top of the MBL and into the free troposphere. In the case of the prefrontal regime, it is likely that the majority of these clouds originate above the MBL. Both clusters are defined as having positive forcing due to strong upward vertical motion at 500 and 850 mb. These clusters also have positive mean dBZ values and are composed of the FCBH and LWP outliers. FCBH and LWP mean values for these clusters are considered outliers because the mean values are approximately 2.2 times higher (FCBH) and 5.8 times higher (LWP) than the next closest regime. Deep MBL clusters occur only 8% of the time, as shown in Figure 4, and are by far the least occurring of any cluster. The susidence inversion is generally not present during these clusters, coinciding well with the inversion being present more than 90% of the time during CAP-MBL (REM12).

The first deep MBL regime has the highest cloud bases and is called the prefrontal regime. With a mean FCBH of 2764 m, many of the cloud bases in this regime may originate above the traditinal low cloud height of 3 km and are double the height of any other cluster. Figure 10.a depicts a prefrontal synoptic environment due to an upstream

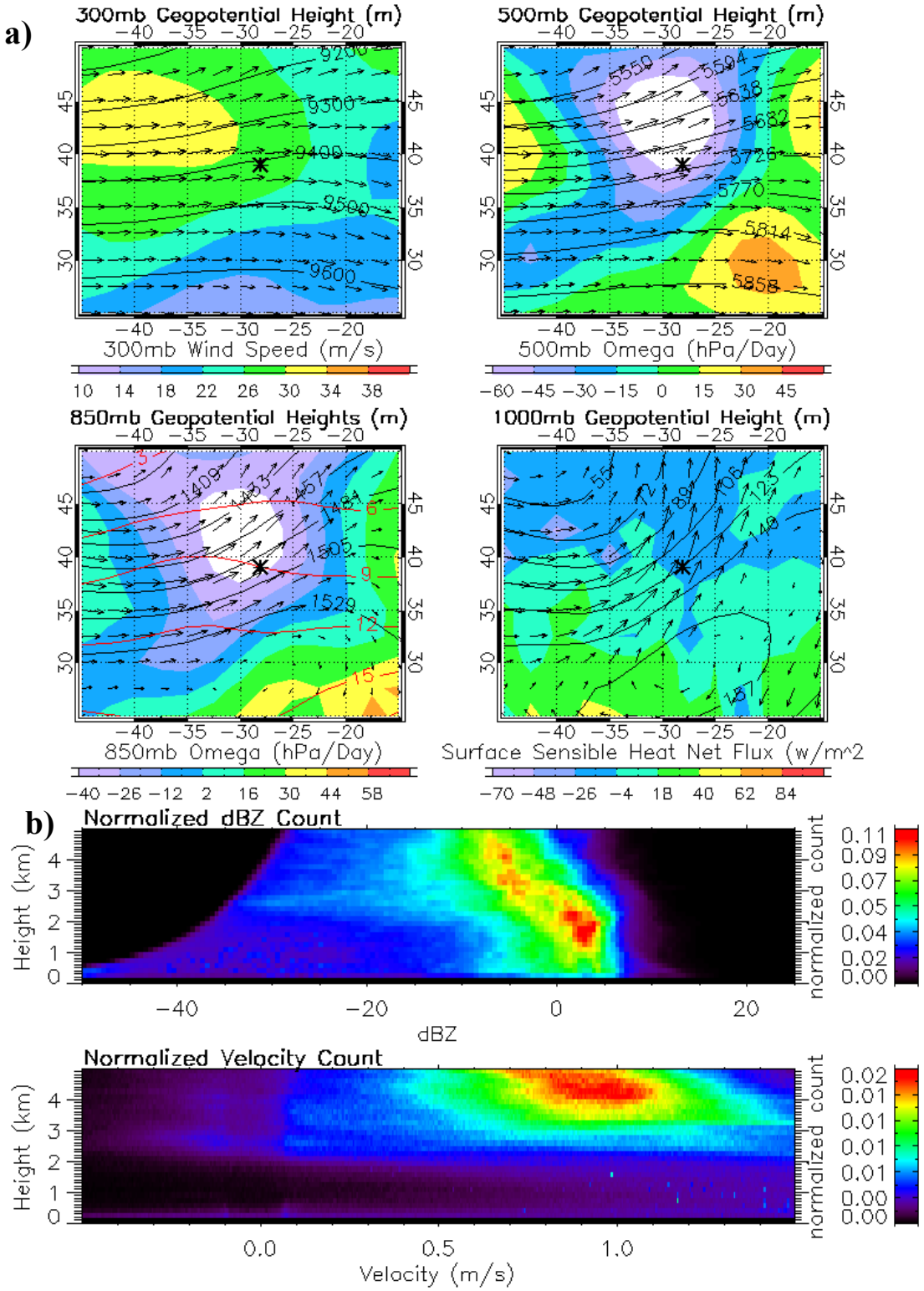

Figure 10. Prefrontal cluster. (a) NCEP/NCAR Reanalysis, the asterisk marks GRW. All black contours show heights at the respective pressure levels with a red contour for temperautre at 850 mb (bottom left). Shading is wind speed (top left), Omega (top right and bottom left), and Surface Sensible Heat Flux (bottom right). (b) Normalized CFADs for reflectivity (top) and MDV (bottom). Positive MDV is downard.

jet streak, the strongest upward vertical motion of any cluster, upstream troughing and downstream ridging, warm air advection at 850 mb, and strong southwest flow near the surface. Per Figure 4, these clouds have glaring maximums in the transition seasons when synoptic fronts are most common over the north atlantic (Hasanean et al. 2004). Figure 10.b shows the depth of these clouds in the dBZ and MDV CFADs along with the a high concentration of dBZ counts at a height below the average FCBH. This is likely due to the prefrontal precipitation below cloud base as shown by the decrease in dBZ values with height.

The final of the seven clusters is the deep precipitating cluster. This cluster only occurs during 4% of the cluster sample but would likely be more frequent if hours where the wet window occurred more than 90% of the time were included in the analysis. As conducted, many hours of heavy precipitation were not included due to the wet window corrupting LWP values. Still, it is likely that some of the LWP values used to calculate this cluster LWP mean were missed by the wet window flag and were corrupted, since the mean is roughly six times higher than the next highest cluster LWP mean. The standard deviation is also the highest at roughly four times the nearst LWP standard deviation. Overall, the high LWP values confirm that these clouds are deeper and more heavily precipitating than other clusters. Mean dBZ values are rougly the same as with the precipitating Cu/Sc cluster, but Figure 11.b shows much less spread than with the precipitating Cu/Sc cluster and high count concentrations at much higher dBZ values. As with the prefontal regime, this cluster shows a decrease in dBZ values with height but also has high concentrations at low heights, indicative of larger drops at the lowest heights and precipitation reaching the ground. The lack of dBZ counts as high as the

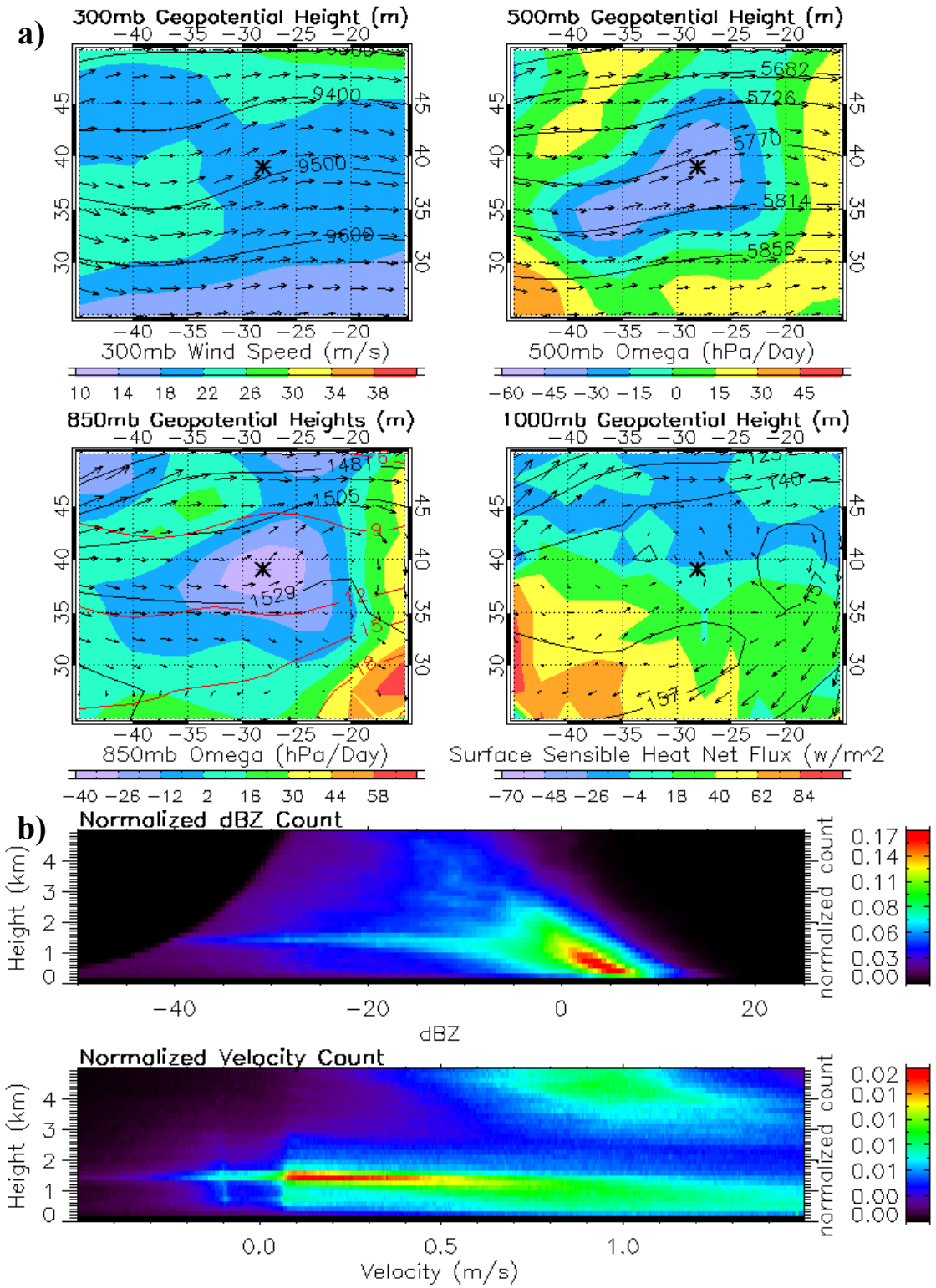

Figure 11. Deep precipitating cluster. (a) NCEP/NCAR Reanalysis, the asterisk marks GRW. All black contours show heights at the respective pressure levels with a red contour for temperautre at 850 mb (bottom left). Shading is wind speed (top left), Omega (top right and bottom left), and Surface Sensible Heat Flux (bottom right). (b) Normalized CFADs for reflectivity (top) and MDV (bottom). Positive MDV is downard.

prefrontal regime could be the result of attenuation due to heavier precipiation. Figure 11.a paints a convincing picutre for a synoptic low pressure system with troughing at all levels, upward vertical motion, and a closed low in the near surface wind flow. Secondary peaks in Figure 4 depict a winter spike in occurrence that is in accordance with the synoptic low pressure. What is interesting is the overall peak of occurrence during the month of July. This is likely the result of occasional deep summer convection from island surface heating or other effects. In order for deep convection to occur, the subtropical high must weaken and while this is not common during the summer, neither is the overall occurrence of this cluster. Low MDV values compared to the precipitating Cu/Sc could indicate smaller drop sizes in comparison to that regime.

Cluster Microphysics Using ARM Retrieval

CAP-MBL surface data are used in the bimodal retrieval in order to gain additional understanding about the microphysical parameters of different clusters. The ARM retrieval is used here primarily because it was the ARM surface data that were used to create the cluster analysis. Hence, using the ARM data to retrieve the microphysical cloud properties means the microphysics are coming from the same clouds that were used to deduce the cloud regime in the cluster analysis. Direct A-train overpasses, even if they occur during the same hour, have the possibility of observing different cloud types when compared to the CAP-MBL data as clouds beyond the range of the CAP-MBL equipment and observing site would be included. The ARM data also have a much finer spatial and temporal resolution, which allow for a highly detailed progression of clouds as they pass over the site. For these reasons, using the A-Train retrieval could produce less consistent and accurate results.

Due to the strengths and limitations of the current bimodal retrieval as outlined in the methods section and to be reviewed here, the microphysics of only three of the seven cloud regimes will be discussed. These three are the weakly precipitating Sc/Cu, the precipitating Cu/Sc, and the drizzling Sc/St. The retrieval algorithm is configured for the MBL and liquid-only hydrometeors, which rules out both of the deep MBL clusters as they frequently extend above the freezing level. These clouds also often have multiple cloud layers, which is a limitation of the algorithm. The two fair weather Cu clusters are not used because the primary focus of this study is on clouds with a greater propensity to precipitate. Case studies with the fair weather Cu clusters will be completed in future work. Additionally, the fair weather Cu clusters are not used here as they would not be ideal for a comparison of both ARM and the A-train retrieval. This is due to the partial beam filling issue of the A-Train. The three case studies that are a part of this study are all afternoon cases with good A-Train overpasses, although they will not be compared to A-Train retrieval data in this section. These cases were selected because they are within the closest 30% of cases to their respective cluster means, meaning they are one of the 30% of cases whose means are closest to the cluster centroid means shown in Figure 3. The cases were also selected because multiple hours surrounding each case study belonged to the same cluster and many of those hours were also in the closest 30% to the cluster centroid. Nine microphysical variables are plotted for each case study for the three clusters and in addition to typical cloud microphysics, these plots also show how r_e and R differ based on retrieved vertical motion.

The nature of case studies means that any trends or conclusions gleaned from these case studies are preliminary and applicable only to these particular cases.

Additional case studies and overall statistics will need to be completed for a more definitive understanding of microphysical differences between cloud regimes. Case studies do serve the important purpose of creating initial theories that can be tested with more data. Uncertainty measurements for a vertical profile of minimal precipitation from an hour of the weakly precipitating Sc/Cu case study are presented in Figure 12. It is important to note that these uncertainties are only for a single profile within the case study hour, and that other profiles will have varying degrees of uncertainty. When all the profiles are combined for an hour, the overall uncertainty decreases. Therefore, Figure 12.b is meant to only give a general idea of uncertainty during a period of very weakly precipitating Sc. The LWC plot in Figure 12.b shows that during this profile, LWC increased with height and that the uncertainty increased with height as well. Cloud r_e values above approximately 1500 m were relatively constant with height and the associated uncertainty was roughly 5 micrometers. Uncertainty estimates of R in the bottom left plot of Figure 12.b also tended to be larger with larger R values and ranged from < 1 mm day^{-1} to approximately 2 mm day^{-1}.

Weakly Precipitating Sc/Cu Microphysics

The time chosen for the weakly precipitating Sc/Cu cluster is 27 Jul 2010. The afternoon hours of 1300 to 1400 and 1400 to 1500 UTC were chosen for this case study due to being close to the weakly precipitating Sc/Cu cluster centroid (mean), with 1300-1400 being closer than 1400-1500. This time frame also has a good A-Train overpass as previously mentioned. Visually, the clouds also represent what is expected from this cluster. This day appeared typical of mid- to late summer MBL synoptic and thermodynamic conditions, which resulted in Sc occurring for most of the day. Figure

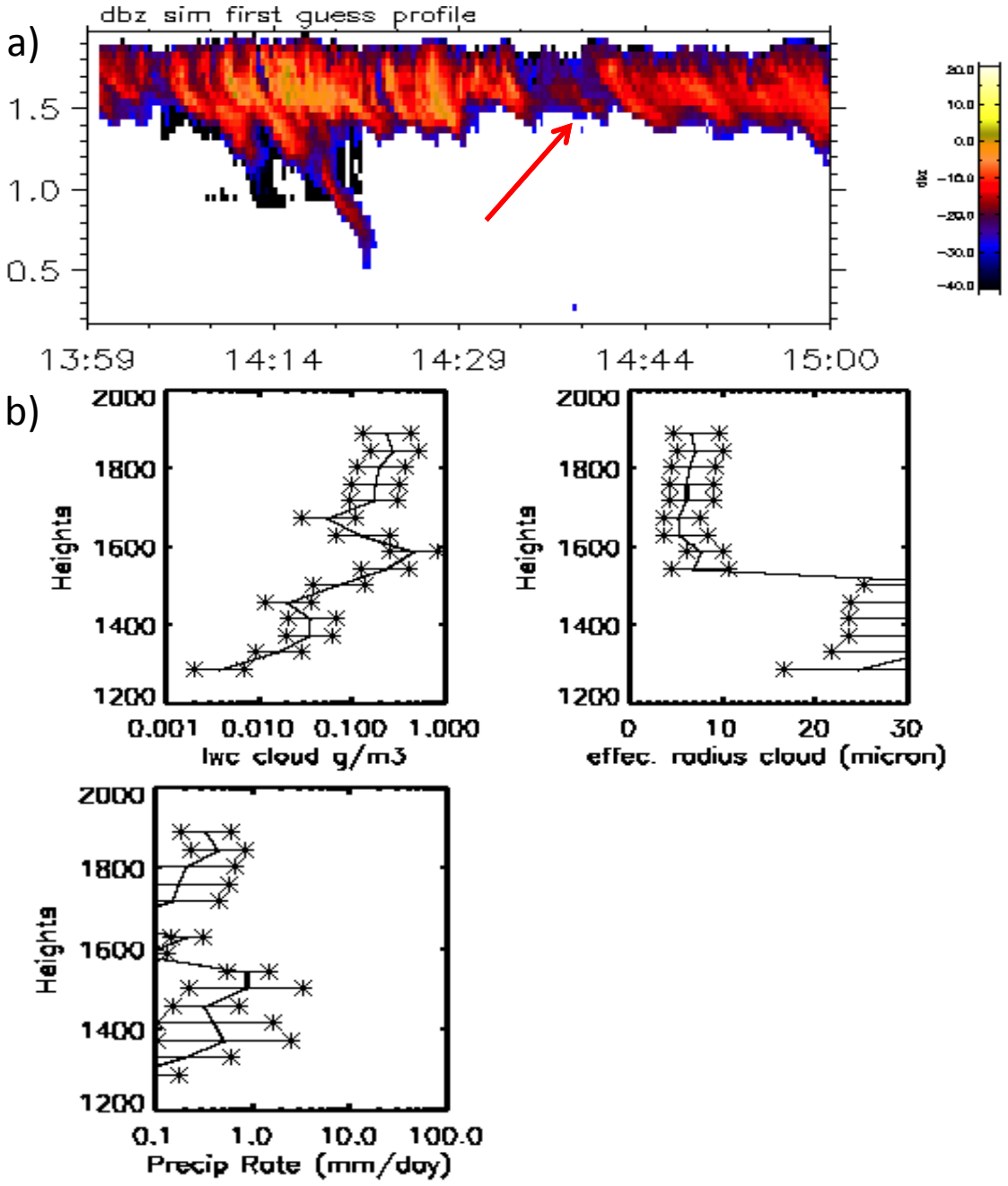

Figure 12. Uncertainty estimates for a profile within the weakly precipitating Sc/Cu cluster case study. (a) Hourly retrieved dBZ values with an arrow used to identify the time stamp of plots used in part b. (b) Uncertainty as a function of height at for the profile occurring at roughly 1438 UTC. Top left is Cloud LWC, top right is cloud r_e and bottom left is R.

13.b indicates a constant Sc deck throughout the 1300 to 1500 UTC timeframe with a transition from thinner, higher-based Sc, to thicker, lower-based Sc as time progressed. Cloud tops of roughly 1.9 km are indicated by dBZ values and as expected, this also matches the base of the radiosonde observed subsidence inversion. Most notable are the thicker clouds at roughly 1405 and the resulting lower bases and higher dBZ values. Detectable dBZ values extend lower beneath cloud base during this time, indicating heavier virga. Also of note is a very thin lower cloud layer that appeared sporadically from 1340 to 1440. Overall, the hour from 1300 to 1400 (first hour) is dominated by thinner clouds with lower dBZ values when compared to that of 1400 to 1500 (second hour).

Figure 13.a shows the microphysical quantities for this case study with the different colors representing the plots and means for the first and second hours. All values represented in these nine plots are obtained from the retrieval algorithm and the histograms represent the occurrence of different values at all heights and times during the applicable hour. Printed mean values are calculated from the values plotted in the histograms and not from the entire possible population. By nature, LWC, N_d, r_e, and R values are sampled where hydrometeors are present. Vertical velocity is a hydrometeor biased conditional sampling of the vertical motion of the air within the column.
Also shown in the center row of Figure 13.a are three plots for cloud mode r_e. These three plots represent information about the maximum sized cloud mode hydrometeors within the vertical column of each radar profile. This is labeled as the column maximum cloud mode r_e. The middle and right plots in this row show column maximum cloud mode r_e in both updraft and downdraft conditions. The updraft plot (middle) contains

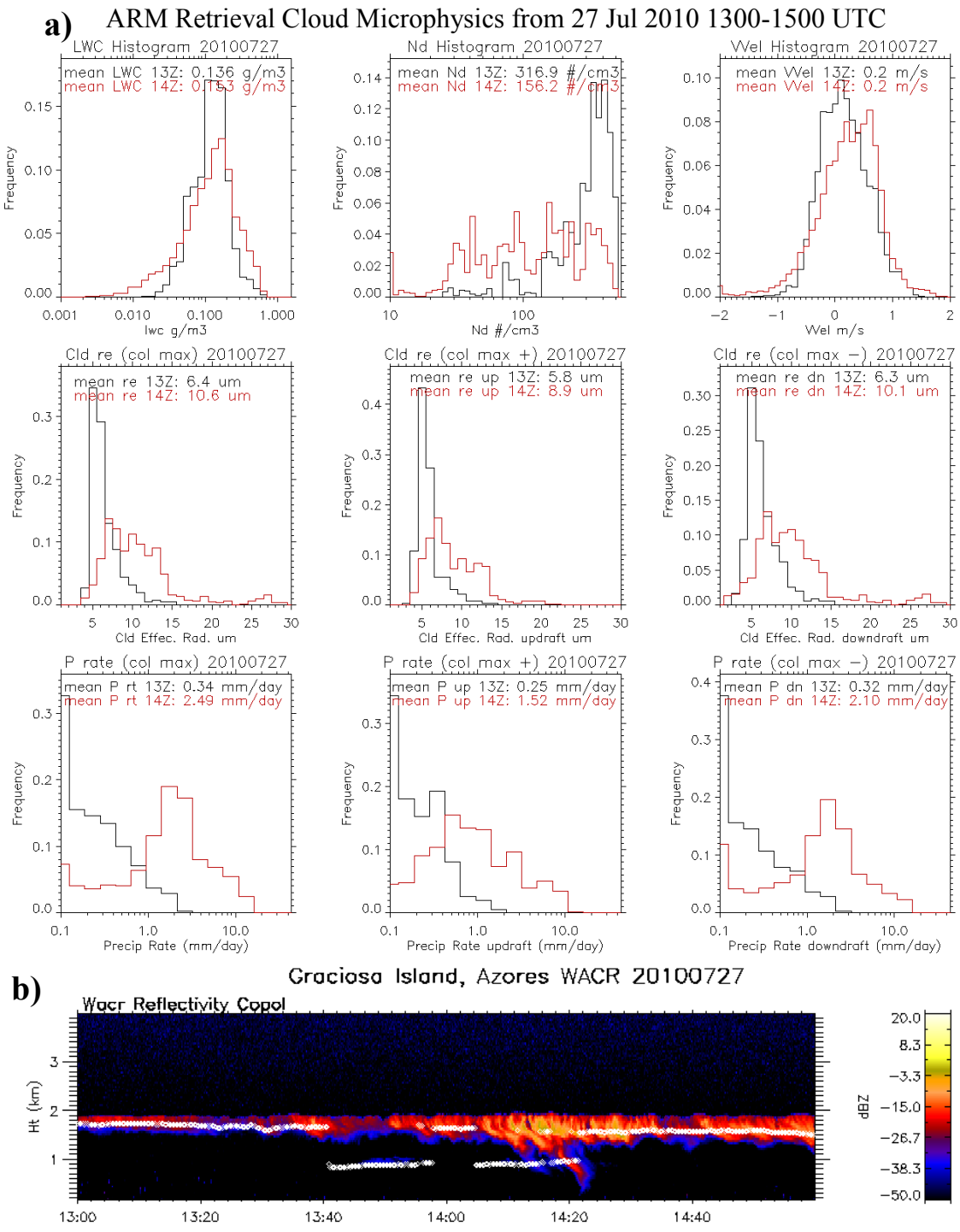

Figure 13. GRW data for 27 Jul 2010. (a) Retrieved cloud microphysical parameters for 1300-1400 (black) and 1400-1500 (red) UTC. The top row of plots show entire column LWC, N_d, and vertical velocity (positive is downward). The middle row has column max cloud mode r_e for the entire hour, updraft, and downdraft portions. The bottom row has column max precipitation rates (R) for the entire hour, updraft, and downdraft portions. (b) WACR dBZ values for 1300-1500 UTC with white circles indicating FCBH.

each column's maximum sized cloud mode hydrometeors that correspond to an area of upward vertical velocity of greater than 2 cm s^{-1}. The downdraft plot (right) data follow the same method as the updraft, except the threshold is now for downward vertical velocities greater than 2 cm s^{-1}. Because it is likely that some of the values used to calculate the overall column maximum r_e (left plot) are found in areas of negligible fall speeds, the mean values of the overall column maximum r_e will not always be in-between the mean values of the updraft and downdraft. The bottom row of Figure 13.a contains the overall column maximum R (left) as well as the updraft column maximum R (middle) and downdraft column maximum R (right). The methodology for these plots of R is the same as the methodology used for the three corresponding column maximum cloud r_e plots.

Upon examining the data, one question that arose is how the microphysical quantities might change from one hour to the next as the Sc deck changed. Figure 13.a shows the microphysics for the two respective hours in question and confirms that changes in the cloud microphysics also occurred. Most glaring are the stark differences in N_d with a dramatic mean N_d reduction of more than half from one hour to the next. Before discussing the potential causes of this reduction, some may question the first hour mean N_d value of 317 cm^{-3}. This value is higher than the typical remote maritime environment of 50 to 100 cm^{-3} given by Wallace and Hobbs (2006) and average annual value of approximately 90 cm^{-3} over the Azores (Wood et al. 2014). However, Wood et al. (2014) show CCN values in excess of 325 cm^{-3} were recorded on many occasions during CAP-MBL and that these high concentrations can be traced to origins in North America, Europe, and Africa (Honrath et al. 2004). CCN values measured by the surface

aerosol observing system (SAOS) based at GRW during the late morning of 27 Jul 2010 ranged from 250 to 400 cm^{-3}. However, a quality assurance issue that occurred on the SAOS for much of the time from 1300 to 1500 UTC means that a direct comparison of these SAOS values with the retrieved N_d values should be done with caution. Nonetheless, the retrieved N_d values are very plausible. Possible reasons for this apparent decrease in N_d will now be explored. Under most conditions, little if any cause and effect relationships can be made between the microphysical properties between two hours because advection may cause the air masses to be entirely different. For these particular hours, however, there is evidence that advection may have been very weak. For winds above the surface, the 1200 and 1800 UTC soundings measured the wind field as calm up to 500 hPa. For surface winds, the first and second hours recorded winds of 2-4 m s^{-1} that shifted from the north to northeast. If advection throughout the column is assumed to be negligible, then the most plausible theory for the dramatic reduction in N_d from the first to second hour is that autoconversion of cloud drops during the first hour was followed by the accretion and savaging of smaller cloud drops by precipitation drops during the second hour. A change in hydrometeor sizes did occur from the first to second hour as cloud-mode r_e values in Figure 13.a increased both in the mean (by a factor of roughly 1.5) and in the distribution. Not shown in Figure 13.a are r_e values for precipitation mode hydrometeors only. The mean of these values rose by a factor of 1.4 from the first hour to the second hour. Also not shown are precipitation mode N_d values, which rose slightly from the first hour to the second. If the same air mass was over GRW for these two hours, then the changes in r_e and N_d provide evidence for growth by autoconversion as cloud drop sizes increased and then a switch to accretion as cloud drop

N_d values fell and precipitation mode r_e values increased. Finally, R increased rapidly from the first to second hours as hydrometeor sizes grew, downward vertical motion increased slightly, and virga intensity increased. However, it is also possible that some advection was present at the surface and that the change in N_d can be attributed to the surface winds. If this is the case, then these results are consistent with the 2nd aerosol indirect effect where the air mass remains the same and lower N_d values lead to larger sizes and higher R. Regarding the large increase in R from the first hour to the second hour, the second hour R increased into a realm similar to that experienced during the drizzling Sc/St cases. However, due to factors such as LWP, cloud base height, and LTS-900, the second hour remained in this cloud regime.

Much work has been done to study the suppression of precipitation as N_d increases in MBL clouds. These studies have included field campaign observations of Sc by Wood (2005), satellite observations of MBL clouds by Leon et al. (2008), modeling of Sc by Ackerman et al. (1995) and modeling MBL Cu by Jiang et al. (2010). The results for the two hours discussed on 27 Jul 2010 do support the idea that a higher N_d results in lower R and vice versa, but only if these changes are not due to advection. The theoretical basis for a decrease in R as N_d increases comes from the 2nd aerosol indirect effect mentioned previously. An area of current research is whether the relationship between high N_d and low R values is a cause and effect relationship or rather just a matter of coincidence with both situations occurring at the same time. A speculative theory about the connection between N_d and R is that large N_d values may suppress R initially, but that this situation can change with time. This could theoretically occur as an air mass of high N_d has slower initial hydrometeor growth by auto-conversion than would be

observed in an air mass with lower N_d, but then reaches a critical growth threshold and accretion takes over. Once accretion takes over, scavenging occurs and the large N_d values provide a source for droplet growth. While the accretion process of precipitation drops collecting smaller cloud drops is not dependent on N_d, the accretion process should act to decrease N_d to some degree. In addition, it has been suggested that self-collection, or the act of large precipitation drops collecting smaller precipitation drops, is proportional to N_d and that the self-collection stage of precipitation growth can increase in a higher N_d environment (Savic-Jovcic and Stevens 2008). While sufficient data are not available here to confirm or deny this theory, it is plausible that with the necessary time and conditions, initially high N_d values could aid in high values of R.

Precipitating Cu/Sc Microphysics

The precipitating Cu/Sc case study occurred on 7 Nov 2010. This case was chosen for the same reasons as the weakly precipitating Sc/Cu cases on 27 Jul 2010. In contrast to the weakly precipitating Sc/Cu case studies, only the hour of 1400 to 1500 UTC is analyzed for this cluster. This was done in order to focus on certain aspects of the microphysics for this particular hour rather than comparing two adjoining hours. The area was dominated by high-pressure synoptic conditions with a closed high just to the northwest of GRW and the base of the subsidence inversion located near 1400 m. Low level winds were out of the east through northeast and were advecting clouds from that direction as shown in Figure 14.b. By comparing Figure 14.a and 14.b, the overcast clouds to the west of GRW appear to be the overcast Sc detected by radar prior to 1400 UTC. The clouds then transition to a more cumuliform cellular structure at roughly 1420 UTC and satellite imagery shows these clouds over and upstream of GRW. The clearing

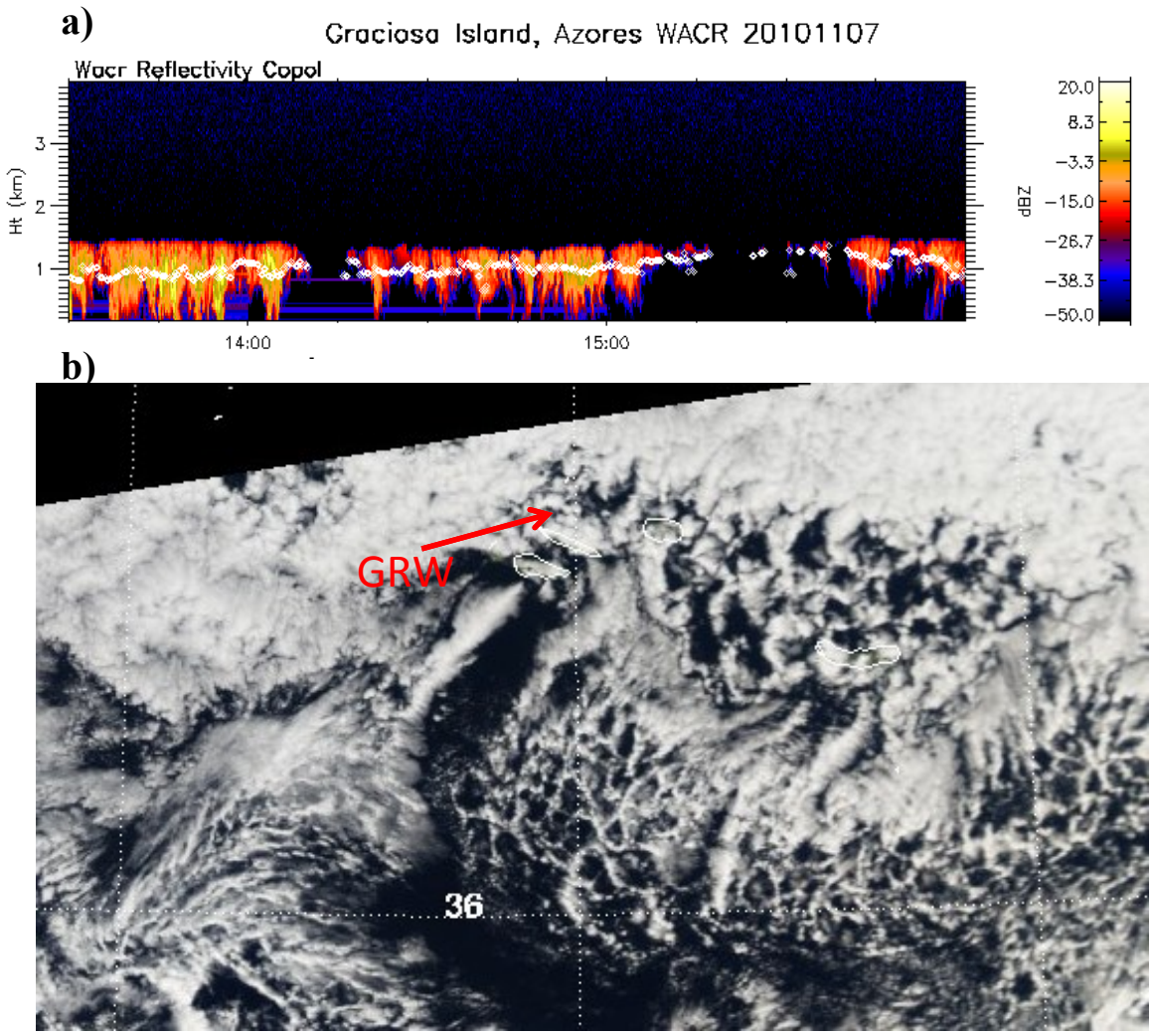

Figure 14. Conditions over GRW on 7 Nov 2010. (a) MODIS visible imagery at 1510 UTC (b) WACR dBZ profile for 1330-1600 UTC with white circles indicating FCBH.

to the east of GRW is likely the break in clouds detected by radar from 1515 to 1540 UTC. Precipitation below cloud base is evident when considering dBZ returns below cloud base in Figure 14.a. dBZ values higher than -15 are visible down to the surface on the WACR plot at roughly 1405 UTC, but precipitation is not evident on the Total Sky Imager (TSI) and surface-based precipitation detection was not deemed reliable during this time.

Figure 15.a lays out the retrieved microphysics for the case study hour. These nine plots follow the same methodology as the nine plots used in Figure 13.a. LWC in the top left shows a predominately Gaussian-like distribution. N_d values are very close to what would be expected over a remote marine environment and are not significantly different than what was observed during other hours of this cluster. R values are higher than in the weakly precipitating Sc/Cu case study but are the lowest of the precipitating Cu/Sc cases that were sampled as possible case studies. The 7 Nov 2010 case was not precipitating as heavily as some of the other days within this regime but it did exhibit a nice cellular structure. The higher cloud fraction of this case also makes it more easily compared to the A-Train retrieval as the A-Train favors high cloud fractions. Retrieved hydrometeor vertical velocity values in Figure 15.a are also Gaussian-like and are skewed toward downward vertical motion, indicative of an hour where downward hydrometeor motion and conditions favorable for below cloud base precipitation are predominant. This is also shown in the updraft and downdraft values for cloud r_e and R, where downdraft values are higher than updraft values. Downdraft distributions for both cloud r_e and R are also very close to the combined up and downdraft cloud r_e and R distributions, indicative of a downdraft dominated environment.

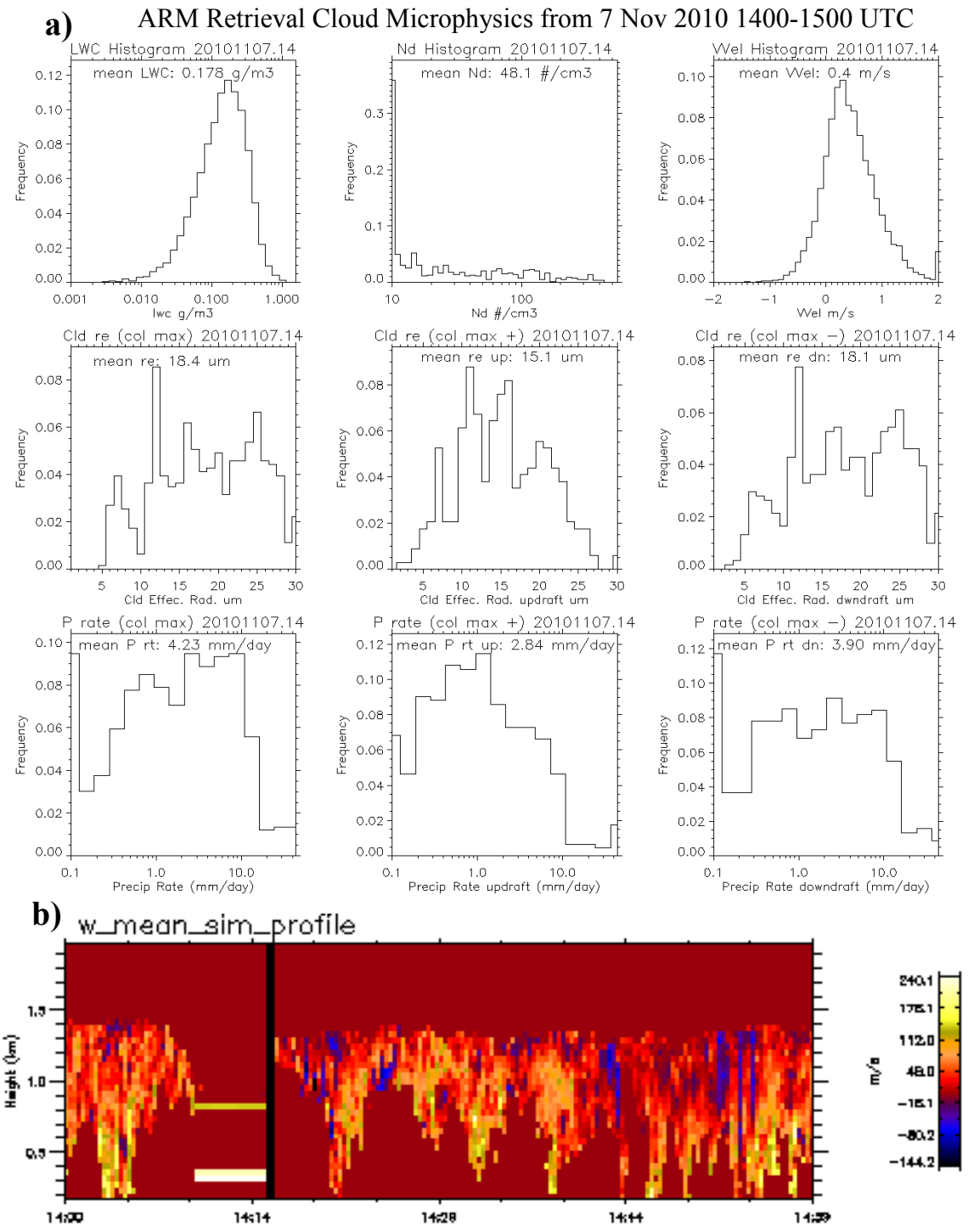

Figure 15. Retrieved GRW microphysical data for 7 Nov 2010. (a) Cloud microphysical parameters for 1400-1500 UTC. The top row of plots show entire column LWC, N_d, and vertical velocity (positive is downward). The middle row has column max cloud mode r_e for the entire hour, updraft, and downdraft portions. The bottom row has column max precipitation rates (R) for the entire hour, updraft, and downdraft. (b) Conditionally sampled vertical velocity for 1400-1500 UTC. Positive is downward.

Although downdrafts are prevalent, updrafts are obviously still present during this hour based on the distribution of vertical velocity. The updrafts and downdrafts play a key role in the development and continuation of these precipitating cloud features (Jensen et al. 2000). In Figure 14.a, multiple cells are distinguishable during the period of 1400-1500 UTC and develop a pattern of a precipitating cell, followed by a very sharp decrease in dBZ values accompanied by no precipitation echoes below cloud base, and then followed by another precipitating cell. This pattern is most apparent from roughly 1420 to 1445 UTC. Figure 15.b shows the retrieved vertical velocity profiles above GRW during this time and highlights the strong downward vertical velocities that are commensurate with the periods of below cloud precipitation. Also evident are updrafts that appear to move over the GRW site prior to a precipitating downdraft and are most concentrated in-between the downdrafts. As expected, these areas of upward vertical motions in 15.b coincide with the areas of decreased dBZ values. Primarily, these updrafts are not as strong as the downdrafts although some parts of the updrafts appear to be close. During the short time frame of this cellular pattern, an updraft occurs over GRW prior to each precipitating cell. Understanding the dynamics that create these updrafts is an important piece in understanding and predicting the precipitation of MBL clouds as well as the potential breakup of overcast MBL clouds (Wood et al. 2005). Possible causes for these updrafts include the surface convergence of downdrafts with the mean environmental flow or other downdraft outflows, similar to cold pool outflows (Snodgrass et al. 2009). While this time series does not allow the differentiation between spatial and temporal changes, some evidence does exist that surface convergence of downdrafts with the mean environmental flow aided in the creation of these updrafts.

Since the environmental flow from the surface up through 700 hPa remains out of the northeast during this entire hour, it is possible that the weak surface outflow from the cell at roughly 1405 converged with the environmental flow to produce the updraft ahead of the 1420 cell. If this surface convergence did occur, then it is possible that this process aided in the formation of precipitation and subsequent downdraft for the 1420 cell, which may have then converged with the environmental flow to produce the updraft at 1425 and the process then continued until 1500 UTC. Further evidence is gathered from the total sky imager, which shows the pattern and propagation of the cells from the northeast. Since a component of each surface outflow must be out of the southwest, or the opposite direction of the environmental wind flow, it is highly plausible that surface convergence between downdrafts and the environmental flow is a catalyst for the updrafts. Another possible source for the updrafts include the surface convergence of outflows from other nearby precipitating cells. Overall, this hour hints at the ability of precipitation to help control the organization of new cloud formation (Jensen et al. 2000).

Drizzling Sc/St Microphysics

The date and time for the drizzling Sc/St cluster case study is 21 Oct 2009 from 1400 to 1500 UTC. This time is selected for the same reasons as the previous two clusters. Synoptically, GRW was on the northern edge of the subtropical high resulting in winds around the high being out of the west over the AMF site. A stationary boundary was located roughly 500 km to the north but GRW was still under the influence of high pressure with the base of the subsidence inversion at roughly 1 km. This hour represents continuous low-level Sc with below cloud base drizzle that gradually intensifies during the period in question. Fundamentally, the overcast and noncellular nature of this Sc deck

is often the result of a low subsidence inversion base that effectively confines available moisture into a smaller volume than was available in the two previous case studies. This shallow MBL is very well mixed and the clouds are strongly coupled to the ocean surface moisture source (Wood and Bretherton 2004). Figure 16.b exhibits a uniform cloud top of roughly 1km and a gradual lowering of FCBH (which is much lower than the previous two clusters) during the case study hour, resulting in the cloud depth increasing due to lowering bases. 1500 to 1530 are included in Figure 16.b to show the cloud transition after the case study hour. dBZ values greater than -15 also lower throughout the hour and eventually reach the surface from 1450 to 1500 UTC. This heavier precipitation just before and after 1500 could be responsible for the transition from closed, to more open cellular convection that appears to take place after 1510 (Wang and Feingold 2009). This transition from closed to open cell Sc is usually accompanied by stronger and larger drizzling cells, which appears to be the case in Figure 16.b beginning at 1500 (Comstock et al. 2007).

Figure 16.a shows the same microphysical variables and follows the same methodology as the previous two case studies. Of note is the dominance by downward vertical motion in the vertical velocity plot. While both updrafts and downdrafts occur in the Sc-topped MBL, downdrafts are more important in the shallow Sc-topped MBL (Krueger et al. 1995). In contrast to Figure 15.b, which shows some updrafts for the deeper and decoupled precipitating Cu/Sc case, a similar Figure for this case study (not shown) is predominately composed of downward vertical motion. When comparing cloud r_e and R for updraft and downdraft sections in Figure 16.a, larger sizes are evident in the downdraft histograms for both variables. Also of note is how the downdraft r_e and

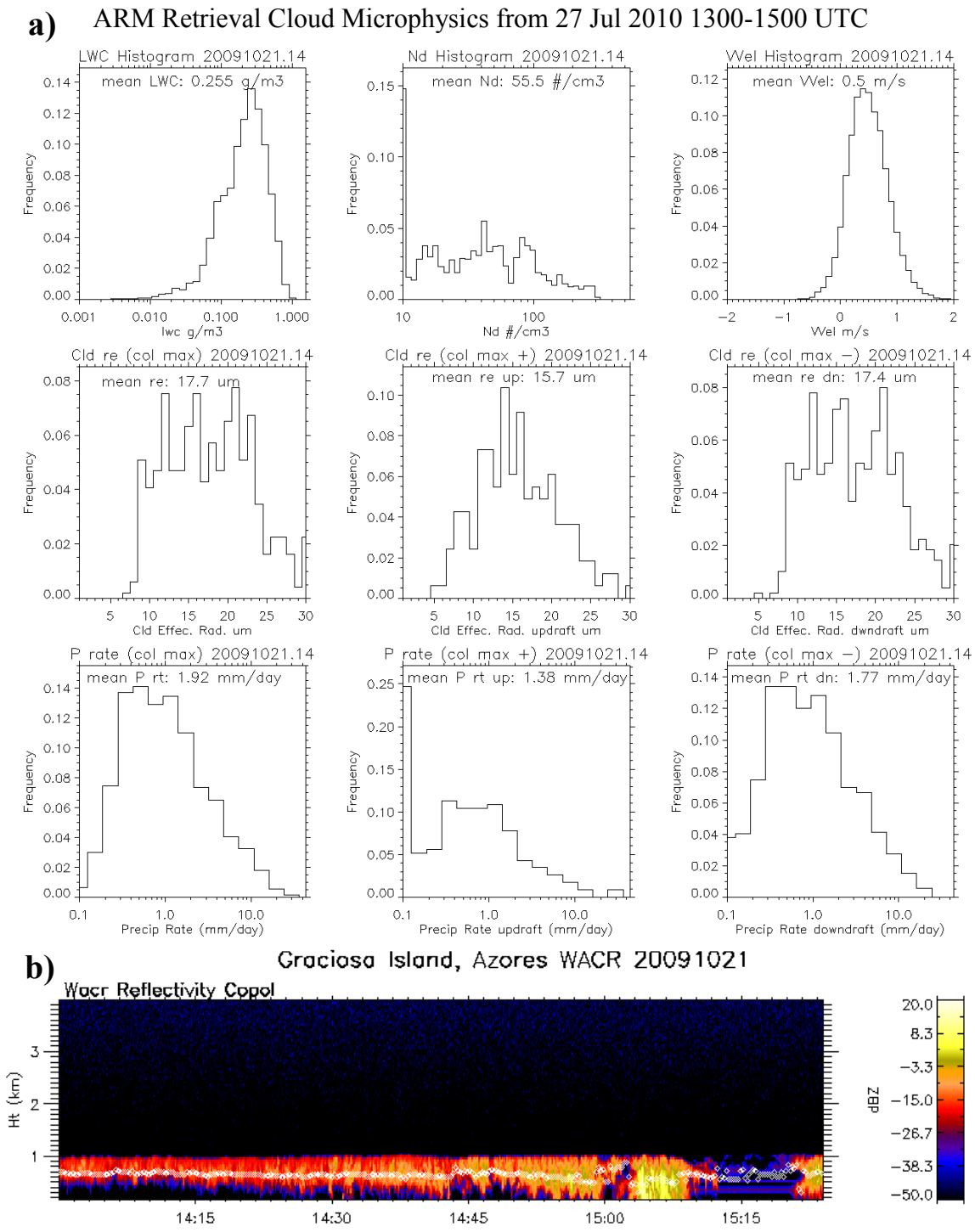

Figure 16. GRW data for 21 Oct 2009. (a) Retrieved cloud microphysical parameters for 1400-1500 UTC. The top row of plots show entire column LWC, N_d, and vertical velocity (positive is downward). The middle row has column max cloud mode r_e for the entire hour, updraft, and downdraft portions. The bottom row has column max precipitation rates (R) for the entire hour, updraft, and downdraft portions. (b) WACR dBZ profile for 1400-1530 UTC with white circles indicating FCBH.

R values are very similar to the overall r_e and R values at the far left of the Figure. This is also the case for the previous two clusters as depicted in Figures 13.a and 15.a and the reasons for this in all three of the case studies will now be explored. The finding of larger R in the downdraft sections of the clouds is consistent with downdrafts to be collocated with the majority of precipitation (Savic-Jovcic and Stevens 2008). Larger values for cloud r_e are also found in the downdraft section. An explanation for this is that being located in the downdraft region gives the cloud mode drops more time to grow, assuming growth begins in the updraft region and then continues in the downdraft region where cloud mode drops transition to precipitation mode.

Less understood are the apparent differences between the weakly precipitating Sc/Cu, precipitating Cu/Sc, and drizzling Sc/St clusters in the degree of difference between r_e and R values in both the updraft and downdraft. Using the mean updraft and downdraft values shown in Figures 13.a, 15.a and 16.a, a comparison between these three clusters can be made. The weakly precipitating Sc/Cu cluster shows an increase by a factor of 1.1 from the updraft cloud r_e to the downdraft cloud r_e and an increase by a factor of roughly 1.3 for R from the updraft to the downdraft. The more heavily precipitating second hour of the weakly precipitating Sc/Cu cluster increases by 1.1 for cloud r_e but by a larger factor of 1.4 for R. The precipitating Cu/Sc cluster r_e increases by a factor of 1.2 from updraft to downdraft while R increases by a factor of 1.4 from updraft to downdraft. Finally, the drizzling Sc/St case shows a small increase in r_e from up to downdraft (factor 1.1) and a small increase in R from up to downdraft (factor of 1.3). While this sample size is extremely small and a much larger sample would be needed to arrive at any conclusions, a very loose connection with these case studies

appears to be that the difference between the updrafts and downdrafts for both r_e and R increases as mean r_e and R increase. This conclusion is plausible as the weakly precipitating clusters have more uniform updrafts and downdrafts along with a more uniform size distribution while more readily precipitating clouds tend toward larger differences in updrafts and downdrafts and have stronger downdrafts.

Three Cluster Microphysical Comparison

The previous three sections have discussed the microphysical parameters for the case studies of the three precipitating Sc, Cu, and St regimes along with a brief comparison of r_e and R in their updrafts and downdrafts. In this section, additional comparisons will be made between the case studies of these three regimes with the aid of Figure 17. Starting first with LWC, the distribution and mean of the weakly precipitating Sc/Cu (WP) appears to have the lowest values followed by the precipitating Cu/Sc (P) and finally by the drizzling Sc/St regime (DZ). This follows the same trend as the mean LWP values in Figure 3 for each of these clusters, which also increase in the same order. One difference is that the LWC values here are much closer for the P and WP clusters while in Figure 3, the LWP values are closer for the P and DZ cases. As is expected to be the case, LWC values are higher for the two more strongly precipitating cases. The N_d comparison summarizes the plots from the previous sections and demonstrates just how large the concentration is for the WP case when compared to the other cases. It should be noted that the high N_d values for this WP case on 27 Jul 2010 were higher than other potential case studies for the WP cluster. However, even the other possible WP case study dates had higher N_d concentrations than the other two clusters. This means that the trend among these case studies of WP being the highest followed by DZ and then P will

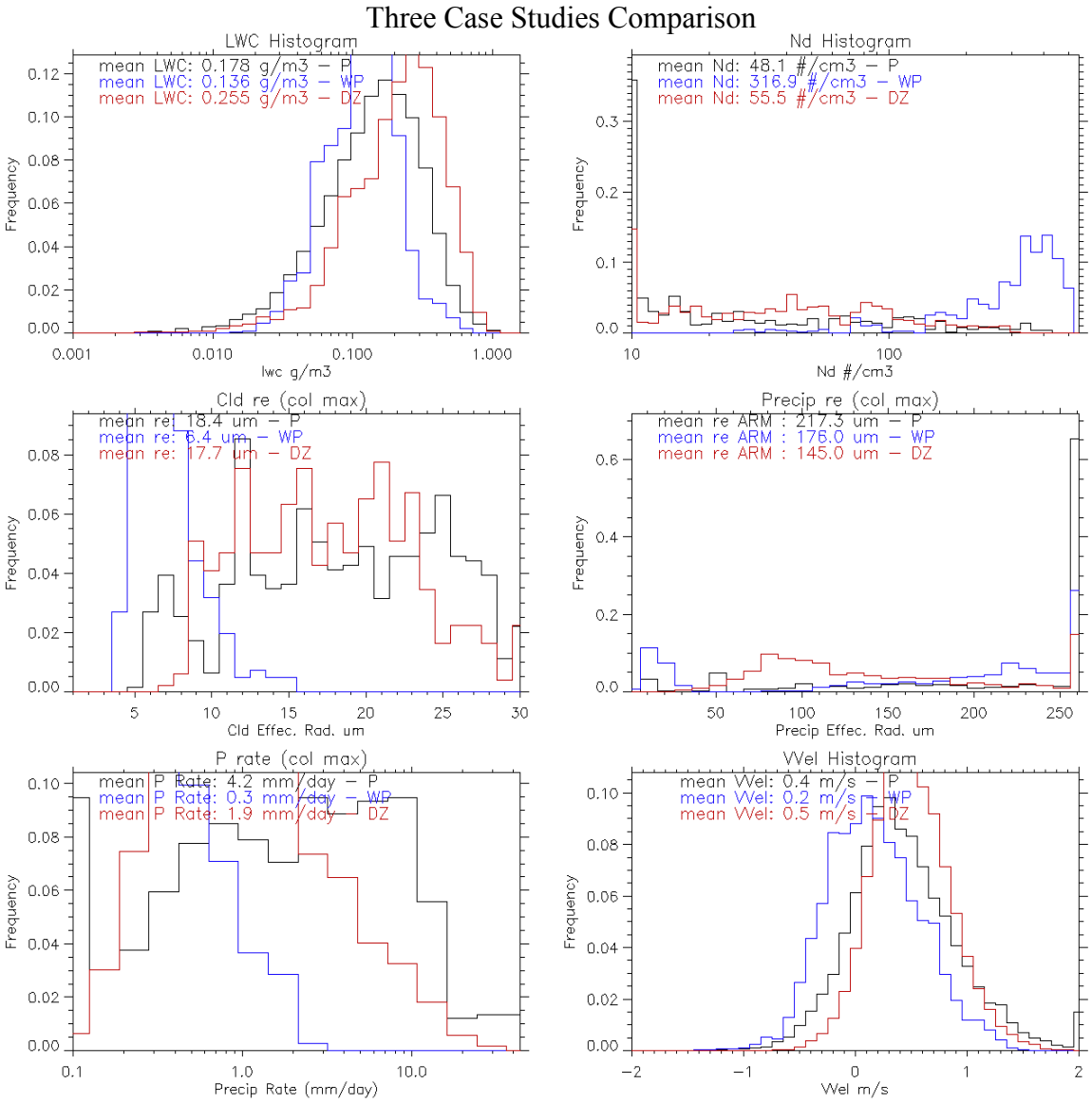

Figure 17. Cloud microphysical comparison for the three precipitating Sc, Cu, and St MBL cloud clusters. Black lines/text are for the precipitating Cu/Sc case of 7 Nov 2010 (P), blue lines/text are for the weakly precipitating Sc/Cu of 27 Jul 2010 (WP), and red lines and text are for the drizzling Sc/St case on 21 Oct 2009 (DZ). The top row has entire column cloud LWC and N_d, followed by column max cloud-mode r_e and precipitation-mode r_e on the second row and finally, column max precipitation rate and entire column conditionally sampled vertical velocity for the bottom row (positive is down).

likely hold in a larger sample size as well. Returning to the three case study hours of Figure 17, a simple negative correlation exists between the trend of lowest to highest N_d values and the trend of highest to lowest R values. As discussed in the WP case study previously, lower N_d values being correlated to higher R values is been well documented in support of the 2nd aerosol indirect effect.

In the middle row of Figure 17 are the cloud and precipitation mode plots for r_e. The cloud mode r_e has maximum values for the P case, followed by the DZ case, and finally for the WP case. This result is also connected to the 2nd aerosol indirect effect where higher concentrations coincide with smaller cloud mode droplets, which in turn coincide with lower values of R. This can occur as the available liquid water is spread over more drops, limiting the growth of the drops and lowering R. Evidence for this correlation between N_d, cloud r_e, and R is found within these three case studies. Figure 17 is the first time that precipitation mode for these case studies is introduced and it shows sizes range from 8 to more than 20 times the size of cloud mode r_e. The benefit of the bimodal retrieval algorithm is that the details of the cloud and precipitation modes are accounted for, rather than mixed together into one size distribution. For precipitation mode r_e, P values are still the highest, but it is followed by the WP case and then the DZ case. This shows that in this sample, precipitation mode r_e values do not follow the 2nd aerosol indirect effect, hinting that this effect is not as applicable to precipitation mode droplets. A possible explanation for precipitation mode not depending on N_d is that once cloud particles have grown to precipitation size, the growth mechanism has switched from auto conversion, which is dependent on N_d, to accretion, which is fairly independent of N_d (Feingold et al. 2013). This means that precipitation sizes will be less dependent on

N_d and could possibly be more dependent on factors like cloud top height, which is higher for both the P and WP cases. The limited size of our study sample means that this finding with precipitation mode r_e might be an anomaly and a larger sample size is needed to draw more robust conclusions. Case study vertical velocities are summarized in the final plot of Figure 17 and DZ values have the largest mean downward motion and are skewed the most toward downward motion. This was mentioned previously due to the dominant nature of downdrafts in this environment. Of note is the tiny peak for the P case study at high downdraft values. These stronger downdrafts are likely due to the more convective nature of the P case study. WP values are skewed more toward updrafts than any other cluster.

As mentioned previously and highlighted in Figure 12, some uncertainty exists in the profiles that make up each of the histograms and mean values of Figure 17. Since Figure 17 is a compilation of all the profiles that make up each respective hour and because the uncertainty in Figure 12 only applies to an individual profile, specific uncertainty will not be applied to the histograms and means of Figure 17. However, the uncertainty in Figure 17 is less than that of Figure 12 due to the number of values combined into Figure 17. It should be noted that while the differences between the different cluster case studies in Figure 17 are not defined as statistically significant due to the some uncertainty in the values, the differences between the case studies are still noteworthy and provide evidence for microphysical differences based on regime. Some of the subtle differences such as those in LWC and vertical velocity are less robust, but the larger differences such as those in R are more robust. Additional case studies for each cluster regime will decrease the uncertainty and enable the significance of these

differences to be explored.

Cluster Microphysics – A-Train vs. ARM Comparison

A small sample size was selected to compare the A-Train and ARM retrievals from the precipitating Cu/Sc regime. This cluster was chosen as it is the most heavily precipitating of the three precipitating Sc, Cu, and St MBL cloud clusters and a priority of this work is to study precipitating cases. This cluster also presented the largest currently available sample size of A-Train overpasses that occurred during an hour that was close to the centroid (mean) of a cluster. In addition to these reasons, the drizzling Sc/St was not chosen because ground clutter would impact the retrieval of these low clouds, which have average FCBH value of 410 m. The goal is to compute the A-Train retrieval for a 5-degree latitude by 10-degree longitude box centered on GRW, compare it to the GRW ground-based ARM retrieval for the same time, and then see what differences there are in the microphysics. This was done for the afternoon A-Train overpass (approximately 1500 UTC) over GRW on following dates in 2010: 5 Mar, 13 Apr, 7 Nov, 9 Nov, and 27 Nov. Comparing the microphysics will improve understanding with regard to the strengths and weaknesses of the satellite-based and ground-based retrieval methods. This information will be used to help describe the retrieval in future studies involving either the ground-based or satellite-based retrievals and will show the versatility of the retrieval methodology.

Figure 18 shows the microphysical histograms and means for the A-Train and ARM cases combined for the five dates. LWC shows the most clearly defined distribution for both retrieval methods with the ARM retrieval nearly a factor of 4 larger than the A-Train retrieval. One reason for the larger values from the ARM retrieval is

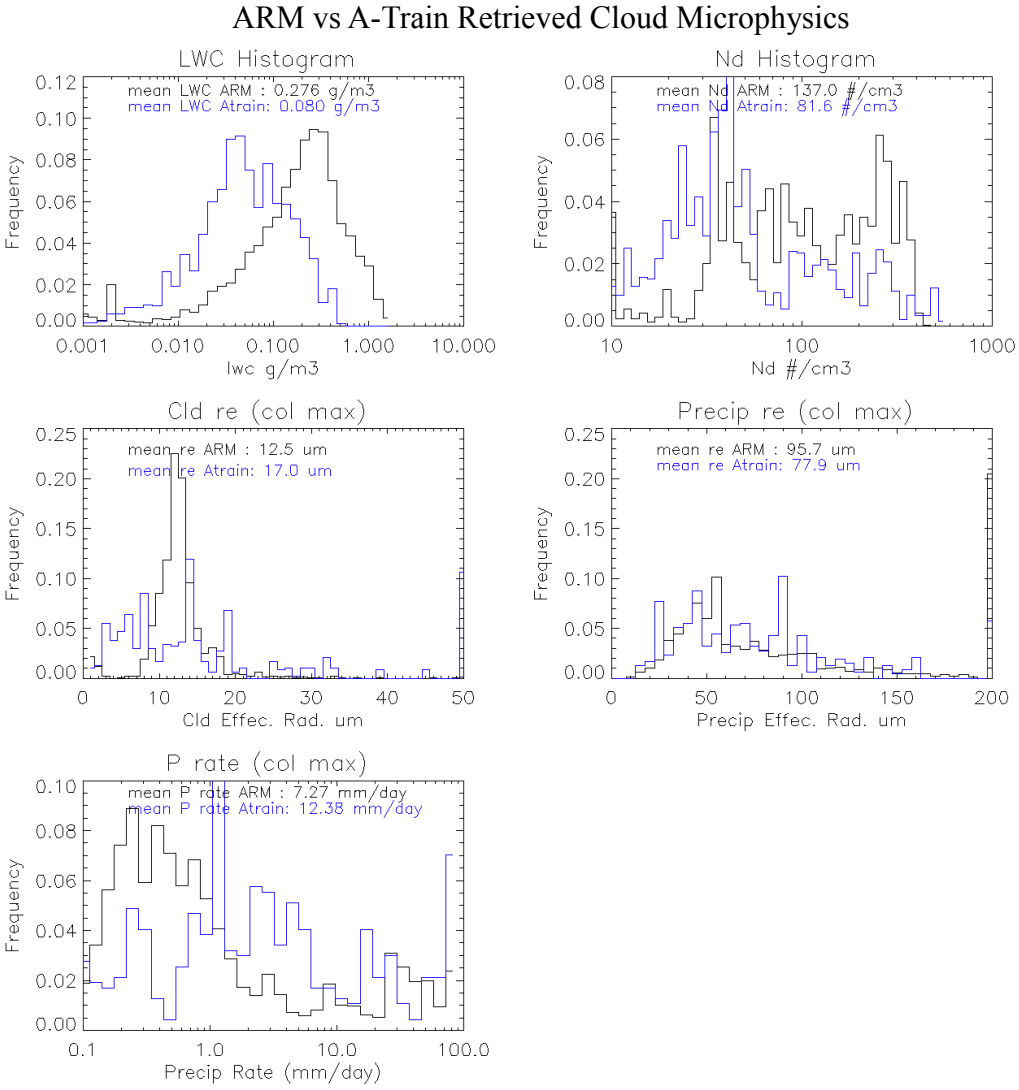

Figure 18. Cloud microphysical comparison for five afternoons of the precipitating Cu/Sc cluster. Black lines/text are results using the ARM retrieval while blue lines/text are results using the A-Train retrieval. The top row has entire column cloud mode LWC and N_d. The second row has column max cloud-mode r_e and precipitation-mode r_e and the bottom row contains column max precipitation rate.

due to the finer vertical resolution of the WACR vs. the A-Train CPR. This finer resolution allows for the ARM retrieval to calculate a more accurate distribution of the liquid water throughout the column. The A-Train's courser vertical resolution could lead to some in-cloud liquid water not being attributed to the cloud and leading to the lower A-Train values. Ground clutter not allowing the base of the cloud to be detected by radar could also play a role. Another reason could be due to the nonovercast nature of this particular cluster. With an average cloud fraction of 70% (although these five cases are likely higher), the broken cloud cover of this cluster means that partial beam filling is occurring to some degree in these cases and noncloudy areas within the A-Train resolution will lower observed radiant fluxes and also retrieved LWC values. The subsequent plot displays larger N_d values for ARM compared to the A-Train. The partial beam filling and vertical resolution limitations of the A-Train should be the reasons A-Train N_d values are lower as well.

Next are the ARM and A-Train r_e values for both cloud and precipitation mode. Here, the two observing platform values are closer to each other than for LWC and N_d. In this case, the A-Train has slightly larger values for the cloud mode r_e while ARM has slightly larger values for the precipitation mode r_e. Values for R in the bottom left of the Figure show larger values for the A-Train. Coupled with the retrieved values for N_d, this follows the pattern observed during the previous section's case studies and is inline with the 2nd aerosol indirect effect. The precipitation mode r_e values are higher for ARM than for A-Train, which does not follow the 2nd aerosol indirect effect. This was also the case for precipitation mode r_e in the previous section, giving additional evidence that there may be a different correlation between N_d, R, and r_e precipitation mode than there is for

N_d, R, and r_e cloud mode.

Returning to the overall differences between the ARM and A-Train retrieved microphysics, the primary reason for these differences is likely that the two retrieval methods are not looking at exactly the same clouds. Looking first at the A-train, it passes over the entire Azores Island area in a matter of minutes and takes a snap-shot of the clouds as it passes over. In contrast, the ARM equipment are stationary and observe the clouds as they advect over the GRW site. They do overlap both spatially and temporally, but this overlap only occurs for a brief moment. While the cloud regime and mean microphysical profiles should be very similar for the greater Azores Islands area, if the exact same clouds are not observed, then differences in the life-cycle of the observed clouds may result in different microphysical quantities. It is also possible that the cloud regime modifies as the A-Train passes over the Azores Islands from south to north. An example of this would be modifying from more broken open cellular Cu, to more closed cellular overcast Sc, and that microphysical quantities modify as the regime does. Overall, the majority of clouds observed by A-Train and ARM are not in the exact same location at the exact same time and this is likely a major reason for the differences in the microphysics of Figure 17.

Future work with the ARM and A-Train comparison will include running more comparison cases in order to see if the differences observed here continue and also to decrease any uncertainty associated with this limited sample. This work will focus on the weakly precipitating Sc/Cu cases, which are categorized by higher cloud fractions and will not be as susceptible to partial beam filling. Ideally, this will quantify the role that partial beam filling plays on the differences in LWC and N_d.

CHAPTER 5

SUMMARY AND CONCLUSION

Data from the ARM CAP-MBL field campaign are analyzed using a K-Means cluster algorithm. Results pertaining to MBL clouds show that these clouds are very common over the Azores and that the most common cloud types are precipitating Sc, Cu, and St with tops that do not extend above the MBL. Results also show that while less common, wide ranges of low clouds are observed over the Azores, including fair weather Cu and deep clouds associated with synoptic systems. Coupled with the findings of Tselioudis (2014), that the MBL clouds observed during CAP-MBL are a good proxy for global MBL cloud occurrence, this implies that the most common MBL cloud regime is precipitating (even if it does not reach the ground), has a temporal cloud fraction of approximately 85%, and has a base of roughly 1 km.

The cluster results also demonstrate that the different cloud types are connected to different large-scale meteorological environments. Factors such as proximity to high and low pressure systems, strength and direction of large-scale vertical motion in the middle and lower atmosphere, low-level temperature advection, and surface sensible heat flux can all differ as the MBL cloud regime changes. The local thermodynamic environment and associated FCBH, along with cloud macrophysical properties such as LWP and cloud fraction, also differ as the MBL cloud regime changes. Of note is the negative correlation between LTS-900 and FCBH for MBL clouds due to the thermodynamic

jump at cloud top and a very weak positive correlation between LTS-900 and cloud fraction. Also shown in CFAD diagrams are the different dBZ and hydrometeor mean Doppler velocity patterns that result from each cloud regime. The CFAD patterns corroborate and display the unique precipitation, cloud height, and hydrometeor motion characteristics of the cloud regimes. The unique information about the respective cloud regimes presented in this study not only paints a picture about that cloud regime, but also aids in identifying the dominant characteristics and cloud type within each respective regime.

Not only does the large-scale meteorological and macrophysical cloud environment modify as the cloud regime changes, but the cloud microphysical environment can as well. The case studies shown in this thesis for three of the seven cluster regimes provide initial evidence for this argument. Case studies for these three clusters show that the highest N_d values, smallest cloud mode r_e, and lowest R values characterize the weakly precipitating Sc/Cu regime. Next is the drizzling Sc/St regime that trended toward smaller N_d values along with slightly larger cloud r_e and R values. Third is the precipitating Cu/Sc regime that had the lowest N_d values followed by the highest cloud r_e and R values. These findings are consistent with the 2nd aerosol indirect effect. Another finding from these three case studies is that precipitation mode r_e does not show the correlation with N_d and R that cloud mode r_e does and additional case studies will be needed in order to verify and provide additional explanations for this finding. Also shown with the weakly precipitating Sc/Cu regime case study is a significant change in cloud microphysical values from one hour to the next. In the absence of advection, this could have occurred due to precipitation and other

modifications of local environment such as increased cloud depth and higher dBZ values. Due to uncertainty in the retrieval, these microphysical results are not definitive but are consistent with current MBL cloud understanding and provide a starting point for additional study and statistics. Uncertainties within the retrieved microphysics will also decrease as more case studies are compiled and statistics are generated.

A comparison of retrieved microphysics with the ARM and A-Train methods are also consistent with the 2nd aerosol indirect effect due to the correlation between N_d, cloud mode r_e, and R. Also evident is the lack of this effect when comparing N_d, precipitation mode r_e, and R. The results of the ARM and A-Train comparison also highlight the differences between these two observing platforms along with their respective limitations. When comparing both of the retrieval methods, the ARM-based retrieval has fewer limitations and should provide a more accurate representation of cloud microphysics, but is also only available for select geographical areas while the A-Train has the potential to provide global coverage. Overall, the differences in the retrieved microphysics do show that both versions of the algorithm produce plausible results for these case studies of the precipitating Cu/Sc regime. Additional case studies with other cloud regimes will further quantify the differences of the ARM and A-Train retrievals and improve the use of both versions of the algorithm.

In conclusion, the resulting connections made here between the large-scale meteorological environment, resulting cloud regime, and cloud macrophysical and microphysical properties can help bridge the gap between the large-scale and small-scale processes that drive cloud production in GCMs. If the initial case study results of how cloud microphysics change with cloud regime hold true with additional statistics, this

information can aid the parameterization of MBL clouds in all types of atmospheric models. Future work will also utilize the retrieval to gather microphysical statistics for the fair weather Cu clusters in order to categorize their microphysical quantities and compare these quantities with those of the precipitating clusters. Further work will also include exploring the relationships between N_d and R in order to quantify the precipitation susceptibility factor (S_o) and compare S_o across the different cloud regimes. This will result in a better understanding of the precipitation processes of shallow marine clouds in the Northern Atlantic and globally.

REFERENCES

Ackerman, A. S., O. B. Toon, and P. V. Hobbs, 1995: Numerical modeling of ship tracks produced by injections of cloud condensation nuclei into marine stratiform clouds. *J. Geophys. Res*., **100** (D4), 7121–7133.

Albrecht, B. A., 1989: Aerosols, cloud microphysics, and fractional cloudiness. *Science*, **245**, 1227–1230.

— —, M. P. Jensen, and W. J. Syrett, 1995: Marine boundary layer structure and fractional cloudiness. *J. Geophys. Res*., **100**, 14209–14222, doi:10.1029/95JD00827.

— —, C. S. Bretherton, D. W. Johnson, W. H. Schubert, and A. S. Frisch, 1995: The Atlantic Stratocumulus Transition Experiment—ASTEX. *Bull. Amer. Meteor. Soc.*, **76**, 889–904.

Ahlgrimm, M., and R. Forbes, 2013: Improving the Representation of Low Clouds and Drizzle in the ECMWF Model Based on ARM Observations from the Azores. *Monthly Weather Review*, **142**, 668-685.

Berry, E., and G. G. Mace, 2013: Cirrus Cloud Properties and the Large-Scale Meteorological Environment: Relationships Derived from A-Train and NCEP–NCAR Reanalysis Data. *J. Appl. Meteor. Climatol.*, **52**, 1253–1276, doi: http://dx.doi.org/10.1175/JAMC-D-12-0102.1.

Bogenschutz, P. A., and S. K. Krueger, 2013: A simplified PDF parameterization of subgrid-scale clouds and turbulence for cloud-resolving models. *J. Adv. Model. Earth Syst*., **5**, 195–211, doi:10.1002/jame.20018.

Bony, S., and J.-L. Dufresne, 2005: Marine boundary layer clouds at the heart of tropical cloud feedback uncertainties in climate models. *Geophys. Res. Lett*., **32**, L20806, doi:10.1029/2005GL023851.

Brooks, M., R. Hogan, and A. Illingworth, 2005: Parameterizing the difference in cloud fraction defined by area and by volume as observed with radar and lidar. *J. Atmos. Sci*., **62**, 2248–2260.

Chen, T., W. B. Rossow, and Y. C. Zhang, 2000: Radiative effects of cloud-type variations. *J. Climate*, **13**, 264–286.

Chen, R., Z. Li, R. J. Kuligowski, R. Ferraro, and F. Weng, 2011: A study of warm rain detection using A-Train satellite data. *Geophys. Res. Lett.*, **38**, L04804.

Christi, M. and P. Gabriel, 2003: *Radiant 2.0: A user's guide*, Colorado State University, 33 pp.

Clement, A. C., R. Burgman, and J. R. Norris, 2009: Observational and model evidence for positive low level cloud feedback. *Science*, **325**, 460–464, doi:10.1126/science.1171255.

Clothiaux, E. E., M. A. Miller, B. A. Albrecht, T. P. Ackerman, J. Verlinde, D. M. Babb, R. M. Peters, and W. J. Syrett, 1995: An evaluation of a 94-GHz radar for remote sensing of cloud properties. *J. Atmos. Oceanic Technol.*,**12**, 201–229.

Comstock, K, S. E. Yuter, R. Wood, and C. S. Bretherton, 2007: The three dimensional structure and kinematics of drizzling stratocumulus. *Mon. Wea. Rev*., **135**, 3767–3784.

Dong, X, and G. G. Mace, 2003: Profiles of Low-Level Stratus Cloud Microphysics Deduced from Ground-Based Measurements. *J. Atmos. Oceanic Technol.*, **20**, 42–53, doi: http://dx.doi.org/10.1175/1520-0426(2003)020<0042:POLLSC>2.0.CO;2

Dufresne, J.-L., and S. Bony, 2008: An Assessment of the Primary Sources of Spread of Global Warming Estimates from Coupled Atmosphere–Ocean Models. *J. Climate*, **21**, 5135–5144, doi: http://dx.doi.org/10.1175/2008JCLI2239.1.

Feingold, G., A. McComiskey, D. Rosenfeld, and A. Sorooshian, 2013: On the relationship between cloud contact time and precipitation susceptibility to aerosol, *J. Geophys. Res. Atmos*., **118**, 10,544–10,554, doi:10.1002/jgrd.50819.

Fox, N. I., and A. J. Illingworth, 1997: The retrieval of stratocumulus cloud properties by ground-based cloud radar. *J. Appl. Meteor.*, **36**, 485–492.

Frisch, A. S., G. Feingold, C. W. Fairall, T. Uttal, and J. B. Snider, 1998: On cloud radar and microwave radiometer measurements of stratus cloud liquid water profiles. *J. Geophys. Res.*, **103,** 23195–23197.

Gerber, H., G. Frick, S. P. Malinowski, H. Jonsson, D. Khelif, and S. K. Krueger, 2013: Entrainment rates and microphysics in POST stratocumulus. *J. Geophys. Res. Atmos*., **118**, 12,094–12,109, doi:10.1002/jgrd.50878.

Ghate, V. P., M. A. Miller, and L. DiPretore, 2011: Vertical velocity structure of marine boundary layer trade wind cumulus clouds. *J. Geophys. Res*., **116**, D16206, doi:10.1029/2010JD015344.

Hahn, C. J., and S. G. Warren, 2007: A gridded climatology of clouds over land (1971–96) and ocean (1954–97) from surface observations worldwide. Numeric Data Package NDP-026E ORNL/CDIAC-153, CDIAC, Department of Energy, Oak Ridge, TN.

Hasanean, H. M., 2004: Variability of the North Atlantic subtropical high and associations with tropical sea-surface temperature. *Int. J. Climatol*., **24**, 945–957.

Hartmann, D. L., M. E. Ockert-Bell, and M. L. Michelsen, 1992: The effect of cloud type on earth's energy balance—Global analysis. *J. Climate*, **5**, 1281–1304.

— —, 1994: *Global Physical Climatology*, Academic Press, 408 pp.

Haynes, J. M., and G. L. Stephens, 2007: Tropical oceanic cloudiness and the incidence of precipitation: Early results from CloudSat. *Geophys. Res. Lett*., **34**, L09811, doi:10.1029/2007GL029335.

Honrath, R. E., R. C. Owen, M. Val Martı´n, J. S. Reid, K. Lapina, P. Fialho, M. P. Dziobak, J. Kleissl, and D. L. Westphal, 2004: Regional and hemispheric impacts of anthropogenic and biomass burning emissions on summertime CO and O3 in the North Atlantic lower free troposphere, *J. Geophys. Res*., **109**, D24310, doi:10.1029/2004JD005147.

Iacobellis, S. F., and R. J. Somerville, 2000: Implications of Microphysics for Cloud-Radiation Parameterizations: Lessons from TOGA COARE. *J. Atmos. Sci.*, **57**, 161–183.

Im, E., S. L. Durden, and C. Wu, 2006: Cloud Profiling Radar for the CloudSat mission. *IEEE Aerosp. Electron. Syst. Mag*., **20**, pp. 15-18.

IPCC, 2013: *Climate Change 2013: The Physical Science Basis. Contribution of Working Group I to the Fifth Assessment Report of the Intergovernmental Panel on Climate Change,* edited by Stocker, T. F., D. Qin, G.-K. Plattner, M. Tignor, S. K. Allen, J. Boschung, A. Nauels, Y. Xia, V. Bex and P. M. Midgley, Cambridge University Press, Cambridge, and New York, NY, 1535 pp.

Jensen, J. B., S. Lee, P. B. Krummel, J. Katzfey, and D. Gogoasa, 2000: Precipitation in marine cumulus and stratocumulus. Part I: Thermodynamicand dynamic observations of closed cell circulations and cumulus bands. *Atmos. Res*., **54**, 117–55.

Jiang, H., G. Feingold, and A. Sorooshian, 2010: Effect of aerosol on the susceptibility and efficiency of precipitation in warm trade cumulus clouds. *J. Atmos. Sci.*, **67**, 3525–3540

Johnson, D. B., 1993: The onset of effective coalescence growth in convective clouds. *Quart. J. Roy. Meteor. Soc.,* **119,** 925–933.

Kiehl, J. T.,1994: On the observed near cancellation between longwave and shortwave forcing in tropical regions. *J. Climate*, **7**, 559–565.

Kistler, R., and Coauthors, 2001: The NCEP-NCAR 50-Year Reanalysis: Monthly means CD-ROM and documentation. *Bull. Amer. Meteor. Soc.*, **82,** 247–267.

Klein, S. A., and D. L. Hartmann, 1993: The seasonal cycle of low stratiform clouds. *J. Climate*, **6**, 1587–1606. LTS is 700-sfc OR 700-SLP

Kollias, P., W. Szyrmer, J. Rémillard, and E. Luke, 2011: Cloud radar Doppler spectra in drizzling stratiform clouds: 2. Observations and microphysical modeling of drizzle evolution. *J. Geophys. Res*., **116**, D13203, doi:10.1029/2010JD015238.

Krueger, S. K., G. T. McLean, Q. Fu, 1995: Numerical Simulation of the Stratus-to-Cumulus Transition in the Subtropical Marine Boundary Layer. Part II: Boundary-Layer Circulation. *J. Atmos. Sci.*, **52**, 2851–2868. doi: http://dx.doi.org/10.1175/1520-0469(1995)052<2851:NSOTST>2.0.CO;2

Kubar, T. L., D. L. Hartmann, and R. Wood, 2009: Understanding the Importance of Microphysics and Macrophysics for Warm Rain in Marine Low Clouds. Part I: Satellite Observations. *J. Atmos. Sci.*, **66**, 2953–2972, doi: http://dx.doi.org/10.1175/2009JAS3071.1

— —, D. E. Waliser, and J-L. Li, 2011: Boundary Layer and Cloud Structure Controls on Tropical Low Cloud Cover Using A-Train Satellite Data and ECMWF Analyses. *J. Climate*, **24**, 194–215, doi: http://dx.doi.org/10.1175/2010JCLI3702.1.

Kummerow, C., W. S. Olson, and L. Giglio, 1996: A simplified scheme for obtaining precipitation and vertical hydrometeor profiles from passive microwave sensors. *IEEE Trans. Geosci. Remote Sens.*, **34**, 1213-1222.

Lacagnina, C., and F. Selten, 2013: A novel diagnostic technique to investigate cloud-controlling factors. *J. Geophys. Res. Atmos*., **118**, 5979–5991, doi:10.1002/jgrd.50511.

Lebsock, M. D., and T. S. L'Ecuyer, 2011: The retrieval of warm rain from Cloudsat. *J. Geophys. Res.*, **116**, D20209, doi: 10.1029/2011JD016067.

— —, T. S. L'Ecuyer, and Graeme L. Stephens, 2011: Detecting the Ratio of Rain and Cloud Water in Low-Latitude Shallow Marine Clouds. *J. Appl. Meteor. Climatol.*, **50**, 419–432, doi: http://dx.doi.org/10.1175/2010JAMC2494.1.

Lee, S., G. Feingold, and P. Chuang, 2012: Effect of aerosol on cloud-environment interactions in trade cumulus. *J. Atmos. Sci.*, **69**, 3607–3632.

Leon, D. C., Z. Wang, and D. Liu, 2008: Climatology of drizzle in marine boundary layer clouds based on 1 year of data from CloudSat and Cloud-Aerosol Lidar and Infrared Pathfinder Satellite Observations (CALIPSO). *J. Geophys. Res*., **113**, D00A14, doi:10.1029/2008JD009835.

Liljegren, J. C., 1994: Two-channel microwave radiometer for observations of total column precipitable water vapor and cloud liquid water path. *Proc. Fifth Symp. on Global Change Studies*, Nashville, TN, Amer. Meteor. Soc., 262–269.

— —, 2000: *Automatic self-calibration of ARM microwave radiometers. Microwave Radiometry and Remote Sensing of the Earth's Surface and Atmosphere,* P. Pampaloni and S. Paloscia, Eds., VSP Press, 433–441.

Lin, J. -L., T. Qian, and T. Shinoda, 2014: Stratocumulus Clouds in Southeastern Pacific Simulated by Eight CMIP5–CFMIP Global Climate Models. *J. Climate*, **27**, 3000–3022, doi: http://dx.doi.org/10.1175/JCLI-D-13-00376.1.

Liu, C., and E. J. Zipser, 2009: ''Warm rain'' in the tropics: Seasonal and regional distribution based on 9 years of TRMM data. *J. Climate*, **22,** 767–779.

Lu, M. L., A. Sorooshian, H. H. Jonsson, G. Feingold, R. C. Flagan, and J. H. Seinfeld, 2009: Marine stratocumulusaerosol-cloud relationships in the MASE-II experiment: Precipitation susceptibility in eastern Pacific marine stratocumulus. *J. Geophys. Res*., **114,** D24203, doi:10.1029/2009JD012774.

Mace, G. G., R. Marchand, Q. Zhang, and G. Stephens, 2007: Global Hydrometeor Occurrence as Observed by CloudSat: Initial Observations from Summer 2006. *Geophys. Res. Lett*., **34,** doi:10.1029/2006GL029017.

— —, 2010: Cloud properties and radiative forcing over the maritime storm tracks of the Southern Ocean and North Atlantic derived from A-Train. *J. Geophys. Res*., **115,** D10201, doi:10.1029/2009JD012517.

Marchand, R. T., G. G. Mace, and T. P. Ackerman, 2008: Hydrometeor detection using CloudSat: An Earth orbiting 94 GHz cloud radar, *J. Atmos. Oceanic Technol*., **25**, 519–533, doi:10.1175/2007JTECHA1006.1.

Mather, J. H., and J. W. Voyles, 2013: The Arm Climate Research Facility: A Review of Structure and Capabilities. *Bull. Amer. Meteor. Soc.*, **94**, 377–392. doi: http://dx.doi.org/10.1175/BAMS-D-11-00218.1

Mechoso, C., R. Wood, C. S. Bretherton, A. Clarke, H. Coe, C. Fairall, J. T. Farrar, G. Feingold, R. Garreaud, C. Grados, J. McWilliams, S. de Szoeke, S. Yuter, and P. Zuidema, 2012: Ocean-Cloud-Atmosphere-Land Interactions in the Southeast Pacific: The VOCALS Program. *Bull. Amer. Meteor. Soc.,* submitted

Mead, J. B., and K. B. Widener, 2005: W-band ARM cloud radar. Preprints, 32nd Int. Conf. on Radar Meteorology, Albuquerque, NM, Amer. Meteor. Soc., P1R.3. [Available online at http://ams.confex.com/ams/pdfpapers/95978.pdf.]

Miles, N. L., J. Verlinde, and E. E. Clothiaux, 2000: Cloud droplet distributions in low-level stratiform clouds. *J. Atmos. Sci*., **57**, 295–311.

Miller, M. A., and B. A. Albrecht, 1995: Surface-Based Observations of Mesoscale Cumulus–Stratocumulus Interaction during ASTEX. *J. Atmos. Sci.*, **52**, 2809–2826, doi: http://dx.doi.org/10.1175/1520-0469(1995)052<2809:SBOOMC>2.0.CO;2

—— —, and Anthony Slingo, 2007: The Arm Mobile Facility and Its First International Deployment: Measuring Radiative Flux Divergence in West Africa. *Bull. Amer. Meteor. Soc.*, **88**, 1229–1244, doi: http://dx.doi.org/10.1175/BAMS-88-8-1229.

Mitas, C. M., and A. Clement, 2006: Recent behavior of the Hadley cell and tropical thermodynamics in climate models and reanalyses. *Geophys. Res. Lett*., **33**, L01810, doi:10.1029/2005GL024406.

Myers, T. A., and J. R. Norris, 2013: Observational Evidence That Enhanced Subsidence Reduces Subtropical Marine Boundary Layer Cloudiness. *J. Climate*, **26**, 7507–7524, doi: http://dx.doi.org/10.1175/JCLI-D-12-00736.1.

Nakajima, T., and M. D. King, 1990: Determinations of the optical thickness and effective particle radius of clouds from reflected solar radiation measurements. Part I: Theory. *J. Atmos. Sci.*, **47**, 1878 -1893.

Nakajima, T. Y., and T. Nakajima, 1995: Wide-area determination of cloud microphysical properties from NOAA AVHRR measurements for FIRE and ASTEX regions. *J. Atmos. Sci*., **52**, 4043–4059.

Nowak, D., D. Ruffieux, J. L. Agnew, and L. Vuilleumier, 2008: Detection of Fog and Low Cloud Boundaries with Ground-Based Remote Sensing Systems. *J. Atmos. Oceanic Technol.*, **25**, 1357–1368, doi: http://dx.doi.org/10.1175/2007JTECHA950.1

Platnick, S., M. D. King, S. A. Ackerman, W. P. Menzel, B. A. Baum, J. C. Riedi, and R. A. Frey, 2003: The MODIS cloud products: Algorithms and examples from Terra. *IEEE Trans. Geosci. Remote Sens.*, **41,** 459–473.

Posselt, D. J., and G. G. Mace, 2014: MCMC-Based Assessment of the Error Characteristics of a Combined Radar-Passive Microwave Cloud Property Retrieval. *J. Appl. Meteor. Clim*., Accepted.

Riehl, C. Yeh, J. S. Malkus, and N. E. LaSeur, 1951: The north-east trade of the Pacific Ocean. *Quart. J. Roy. Meteor. Soc.,* **77,** 598–626.

Randall, D. A., J. A. Coakley, C. W. Fairall, R. A. Knopfli, and D. H. Lenschow, 1984: Outlook for research on marine subtropical stratocumulus clouds. *Bull. Amer. Meteor. Soc*., **65**, 1290–1301.

Rauber, R. M., and Coauthors, 2007: Rain in Shallow Cumulus over the Ocean—The RICO Campaign. *Bull. Amer. Meteor. Soc.,* **88,** 1912–1928.

Rémillard, J., P. Kollias, E. Luke, and R. Wood, 2012: Marine boundary layer cloud observations in the Azores, *J. Clim.*, **25**, 7381–7398, doi: http://dx.doi.org/10 .1175/JCLI-D-11-00610.1

Rossow, W. B., G. Tselioudis, A. Polak, and C. Jakob, 2005: Tropical climate described as a distribution of weather states indicated by distinct mesoscale cloud property mixtures. *Geophys. Res. Lett*., **32**, L21812, doi:10.1029/2005GL024584.

Sharon, T. M., B. A. Albrecht, H. H. Jonsson, P. Minnis, M. M. Khaiyer, T. M. van Reken, J. Seinfeld, and R. Flagan, 2006: Aerosol and cloud microphysical characteristics of rifts and gradients in maritime stratocumulus clouds. *J. Atmos. Sci*., **63**, 983–997.

Slingo, A., 1990: Sensitivity of the Earth's radiation budget to changes in low clouds. *Nature*, **343**, 49–51.

Small, J.D., and P.Y. Chuang, 2008: New Observation of Precipitation Initiation in Warm Cumulus Clouds. *J. Atmos. Sci.*, **65**, 2972-2982.

Soden, B. J. and I. M. Held, 2006: An Assessment of Climate Feedbacks in Coupled Ocean–Atmosphere Models. *J. Climate*, **19**, 3354–3360.

Sorooshian, A., G. Feingold, M. D. Lebsock, H. Jiang, and G. L. Stephens, 2009: On the precipitation susceptibility of clouds to aerosol perturbations. *Geophys. Res. Lett.,* **36,** L13803, doi:10.1029/2009GL038993.

— —, G. Feingold, M. D. Lebsock, H. Jiang, and G. L. Stephens, 2010: Deconstructing the precipitation susceptibility construct: Improving methodology for aerosol-cloud precipitation studies, *J. Geophys. Res*., **115**, D17201,doi:10.1029/2009 JD013426.

Snodgrass, E. R., L. D. Girolamo, and R. M. Rauber, 2009: Precipitation Characteristics of Trade Wind Clouds during RICO Derived from Radar, Satellite, and Aircraft Measurements. *J. Appl. Meteor. Climatol.*, **48**, 464–483.

Stephens, G. L., 1994, *Remote Sensing of the Lower Atmosphere: An Introduction*, Oxford University Press Inc., 544 pp.

— —, and Coauthors, 2002: The CloudSat Mission and the A-Train. *Bull. Amer. Meteor. Soc.*, **83**, 1771-1790.

— —, T. L'Ecuyer, R. Forbes, A. Gettlemen, J.-C. Golaz, A. Bodas-Salcedo, K. Suzuki, P. Gabriel, and J. Haynes, 2010: Dreary state of precipitation in global models, *J. Geophys. Res*., **115**, D24211, doi:10.1029/2010JD014532.

Stevens, B., and G. Feingold, 2009: Untangling aerosol effects on clouds and precipitation in a buffered system. *Nature*, **461**, doi:10.1038/nature08281.

Suzuki, K., G. Stephens, S. van den Heever, and T. Nakajima, 2011: Diagnosis of the warm rain process in cloud-resolving models using joint *CloudSat* and MODIS observations. *J. Atmos. Sci.*, **68**, 2655–2670.

Tselioudis, G., 2014: *Evaluation of SCM and LES simulations using CAP-MBL and satellite retrievals,* Atmospheric System Research Science Team Meeting, Potomac, Maryland, 10 Mar. 2014.

Twomey, S. 1977: The influence of pollution on the shortwave albedo of clouds, *J. Atmos. Sci*., **34**, 1149–1152.

Wallace, J.M., and P. V. Hobbs, 2006: *Atmospheric Science: An Introductory Survey*. 2nd Ed., Academic Press, 483 pp.

Wang, H., and G. Feingold, 2009: Modeling mesoscale cellular structures and drizzle in marine stratocumulus. Part I: Impact of drizzle on the formation and evolution of open cells. *J. Atmos. Sci*., **66**, 3237–3255.

Westwater, E. R., B. B. Stankov, D. Cimini, Y. Han, J. A. Shaw, B. M. Lesht, C. N. Long, 2003: Radiosonde Humidity Soundings and Microwave Radiometers during Nauru99. *J. Atmos. Oceanic Technol.*, **20**, 953–971.

Williams, K. D., and G. Tselioudis, 2007: GCM intercomparison of global cloud regimes: Present-day evaluation and climate change response. *Clim. Dyn*., **29**, 231-250, doi:10.1007/s00382-007-0232-2.

Wood, R. and C. S. Bretherton, 2004: Boundary layer depth, entrainment, and decoupling in the cloud-capped subtropical and tropical marine boundary layer. *J. Climate*, **17**, 3576–3588.

— —, 2005: Drizzle in stratiform boundary layer clouds. Part I: Vertical and horizontal structure. *J. Atmos. Sci*., **62**, 3011–3033.

— —, and C. S. Bretherton, 2006: On the Relationship between Stratiform Low Cloud Cover and Lower-Tropospheric Stability. *J. Climate*, **19**, 6425–6432, doi: http://dx.doi.org/10.1175/JCLI3988.1

— —, and D. L. Hartmann, 2006: Spatial Variability of Liquid Water Path in Marine Low Cloud: The Importance of Mesoscale Cellular Convection. *J. Climate*, **19**, 1748–1764, doi: http://dx.doi.org/10.1175/JCLI3702.1

— —, T. L. Kubar, and D. L. Hartmann, 2009: Understanding the Importance of Microphysics and Macrophysics for Warm Rain in Marine Low Clouds. Part II: Heuristic Models of Rain Formation. *J. Atmos. Sci.*, **66**, 2973–2990, doi: http://dx.doi.org/10.1175/2009JAS3072.1

— —, 2012: Stratocumulus Clouds. *Mon. Wea. Rev.*, **140**, 2373–2423, doi: http://dx.doi.org/10.1175/MWR-D-11-00121.1.

— —, and coauthors, 2014: Clouds, Aerosol, and Precipitation in the Marine Boundary Layer: An ARM Mobile Facility Deployment. Submitted to *Bull. Amer. Meteor. Soc*., September 2013.

Yin, B., and B. A. Albrecht, 2000: Spatial variability of atmospheric boundary layer structure over the eastern equatorial Pacific. *J. Climate*, **13**, 1574–1592.

Yuter, S. E., and R. A. Houze, 1995: Three-dimensional kinematic and microphysical evolution of Florida cumulonimbus. Part II: Frequency distributions of vertical velocity, reflectivity, and differential reflectivity. *Mon. Wea. Rev.*, **123**, 1941–1963.

Zhang, G. J., A. M. Vogelmann, M. P. Jensen, W. D. Collins, and E. P. Luke, 2010: Relating satellite-observed cloud properties from MODIS to meteorological conditions for marine boundary layer clouds. *J. Climate*, **23,** 1374–1391.

Zhao, Y., G. G. Mace, J.M. Comstock, 2011: The occurrence of particle size distribution bimodality in midlatitude cirrus as inferred from ground-based remote sensing data. *J. Atmos. Sci.*, **68**, 1162–1177.